A&A 505, 1221–1232 (2009)
DOI: 10.1051/0004-6361/200912332

Astronomy & Astrophysics

Post-AGB stars with hot circumstellar dust: binarity of the low-amplitude pulsators⋆,⋆⋆

H. Van Winckel[1], T. Lloyd Evans[2], M. Briquet[1,⋆⋆⋆], P. De Cat[1,3], P. Degroote[1], W. De Meester[1], J. De Ridder[1⋆⋆], P. Deroo[1,4], M. Desmet[1], R. Drummond[1,5], L. Eyer[1,6], M. A. T. Groenewegen[1,3], K. Kolenberg[1,7], D. Kilkenny[9], D. Ladjal[1], K. Lefever[1,5], T. Maas[1], F. Marang[10], P. Martinez[10], R. H. Østensen[1], G. Raskin[1], M. Reyniers[1,8], P. Royer[1], S. Saesen[1,†], K. Uytterhoeven[1,11], J. Vanautgaerden[1], B. Vandenbussche[1], F. van Wyk[10], M. Vučković[1], C. Waelkens[1], and W. Zima[1]

[1] Instituut voor Sterrenkunde, K.U.Leuven, Celestijnenlaan 200B, 3001 Leuven, Belgium
e-mail: Hans.VanWinckel@ster.kuleuven.be
[2] SUPA, School of Physics and Astronomy, University of St Andrews, North Haugh, St Andrews, Fife, Scotland KY16 9SS, UK
[3] Royal Observatory of Belgium, Ringlaan 3, 1180 Brussel, Belgium
[4] Jet Propulsion Laboratory, Caltech, 4800 Oak Grove Drive, Pasadena, CA 91109, USA
[5] Belgian Institute for Space aeronomy, Ringlaan 3, 1180 Brussels, Belgium
[6] Observatoire de Genève, 1290 Sauverny, Switzerland
[7] Institut für Astronomie der Universität Wien, Türkenschanzstrasse, 17, 1180 Vienna, Austria
[8] The Royal Meteorological Institute of Belgium, Department Observations, Ringlaan 3, 1180 Brussels, Belgium
[9] Dept. of Physics, University of the Western Cape, Private Bag X17, Bellville 7535, Western Cape, South Africa
[10] South African Astronomical Observatory, PO Box 9, Observatory 7935, South Africa
[11] Laboratoire AIM, CEA/DSM-CNRS-Université Paris Diderot; CEA, IRFU, SAp, centre de Saclay, 91191 Gif-sur-Yvette, France

Received 15 April 2009 / Accepted 3 July 2009

ABSTRACT

Context. The influence of binarity on the late stages of stellar evolution remains an open issue.
Aims. While the first binary post-AGB stars were serendipitously discovered, the distinct characteristics of their spectral energy distribution (SED) allowed us to launch a more systematic search for binaries. We selected post-AGB objects, which exhibit a broad dust excess starting either at H or K, pointing to the presence of a gravitationally bound dusty disc in the system. We initiated an extensive multiwavelength study of those systems and here report on our radial velocity and photometric monitoring results for six stars of early F type, which are pulsators of small amplitude.
Methods. To determine the radial velocity of low signal-to-noise ratio time-series data, we constructed dedicated autocorrelation masks based on high signal-to-noise ratio spectra, used in our published chemical studies. The radial velocity variations were analysed in detail to differentiate between pulsational variability and variability caused by orbital motion. When available, the photometric monitoring data were used to complement the time series of radial velocity data and to establish the nature of the pulsation. Finally, orbital minimalisation was performed to constrain the orbital elements.
Results. All of the six objects are binaries with orbital periods ranging from 120 to 1800 days. Five systems have non-circular orbits. The mass functions range from 0.004 to 0.57 $M_{\odot}$ and the companions are probably unevolved objects of (very) low initial mass. We argue that these binaries must have evolved through a phase of strong binary interaction when the primary was a cool supergiant. Although the origin of the circumstellar disc is not well understood, the disc is generally believed to have formed during this strong interaction phase. The eccentric orbits of these highly evolved objects remain poorly understood. In one object, the line-of-sight grazes the edge of the puffed-up inner rim of the disc.
Conclusions. These results corroborate our earlier statement that evolved objects in binary stars create a Keplerian dusty circumbinary disc. With the measured orbits and mass functions, we conclude that the circumbinary discs seem to have a major impact on the evolution of a significant fraction of binary systems.

Key words. stars: AGB and post-AGB – stars: binaries: general – stars: binaries: spectroscopic – stars: chemically peculiar – stars: evolution

1. Introduction

Post-AGB stars are low- and intermediate-mass stars that evolve rapidly from the asymptotic giant branch (AGB) toward the planetary nebulae phase (PNe), before cooling to form a white dwarf. The processes that govern the transition between the symmetry in the AGB outflows and the observed large variety in geometries of proto-PNe and PNe, are still poorly understood (Balick & Frank 2002; Sahai et al. 2007, and references therein). During the transition time, the star and its circumstellar envelope must

⋆ based on observations collected with the Flemish 1.2 m Mercator telescope at Roque de los Muchachos (Spain), the Swiss 1.2 m Euler telescope at La Silla (Chile) and the 0.5 m and 0.75 m telescopes at SAAO (South-Africa).
⋆⋆ Tables 4–6 are only available in electronic form at http://www.aanda.org
⋆⋆⋆ Postdoctoral fellow of the Fund for Scientific Research, Flanders.
† Ph.D. student of the Fund for Scientific Research, Flanders.

be subject to fundamental and rapid changes in structure, mass-loss mode, and geometry. It is now generally acknowledged that binary interaction in these evolved stars could be responsible for a large fraction of the observed asymmetric nebular morphologies, but direct observational evidence of binarity in PNe is weak (Moe & De Marco 2006; Zijlstra 2007). An analysis of the lightcurves obtained by the OGLE microlensing survey towards the Galactic bulge, inferred a close binary fraction of 12–21% (Miszalski et al. 2009). These data are only sensitive to the detection of systems which underwent a strong orbital decrease during interaction.

Testing the (wide) binary hypothesis is severely limited by the lack of observational information about binarity in PNe and the often very obscured proto planetary nebulae (PPNe), and also by our poor theoretical understanding of AGB evolution in binary systems. A major shortcoming is that detailed studies of individual, often spectacular, evolved objects prevail and systematic studies of a homogeneous sample are lacking. To study late stellar evolution in binary systems, optically bright, less obscured post-AGB stars are ideal candidates, and it has become clear that binarity is indeed very common (Van Winckel 2007).

The first binary post-AGB stars were serendipitously discovered and found to have distinct observational characteristics, including broad dust excesses often starting already at H or K, inferring the presence of both hot and cool dust around the system. It was postulated that this indicates the presence of gravitationally-bound circumstellar material in the system (Van Winckel 2003, and references therein). The most famous example is the Red Rectangle, for which the Keplerian kinematics have been resolved by interferometric CO measurements (Bujarrabal et al. 2005).

These characteristics of their SEDs allowed us to develop a more systematic search for candidate binaries. In de Ruyter et al. (2006), we presented 51 objects and the number of known examples has since increased. The total sample is now a fair proportion of the 326 "very likely post-AGB stars" known in the Galaxy (Szczerba et al. 2007). Our selection criteria focused on infrared colours and resulted in including the RV Tauri stars with a dust excess detected by IRAS, the known binary post-AGB stars and newly characterised objects selected by Lloyd Evans (1999) on the basis of their position in the "RV Tauri" box in the IRAS [12]–[25], [25]–[60] two-colour diagram (see also Maas et al. 2003).

A typical spectral energy distribution is shown in Fig. 1. The stellar flux reprocessed into the infrared is about 50% for this star. The interested reader is referred to de Ruyter et al. (2006) for the SEDs of the complete sample. In all objects of the sample, the dust excess starts at, or very close to, dust sublimation temperature, irrespective of the spectral type of the central star. With a typical luminosity of a post-AGB star, this sublimation temperature edge is within a distance of 10 AU from the central source. We therefore inferred (e.g. Van Winckel 2003) that part of the dust must be gravitationally bound: any typical AGB outflow velocity would bring the dust to cooler regions within years. This time is much shorter than the likely evolutionary timescale of the central object. We argued that the same inner geometry, found in the resolved system HD 44179 (Men'shchikov et al. 2002; Cohen et al. 2004; Bujarrabal et al. 2005), applies to the whole sample, i.e., the objects seem to be surrounded by Keplerian discs of dust.

Our interferometric studies confirm the very compact nature of the circumstellar material (Deroo et al. 2006, 2007). Our Spitzer and ground-based *N*-band spectroscopic data show that dust grain processing is strong, the oxygen-rich dust being dominated by, considerably larger, crystalline silicates (Gielen et al. 2008). Sub-mm bolometric data, which is available for only a few sources, show the presence of large grains in the circumstellar environment (De Ruyter et al. 2005). These large grains have relatively small dust-settling times, probably causing the disc to be inhomogeneous with small hot grains dominating the surface layers and a cooler midplane of mainly large grains (Gielen et al. 2007).

The true structure of those discs, in addition to their formation, stability, and evolution, are not well understood. We therefore initiated an extensive multiwavelength study of those systems. In this contribution, we report on our detailed radial velocity monitoring programme on the 1.2 m Swiss Euler telescope. The complementary photometric monitoring was performed at both SAAO and the 1.2 m Flemish Mercator telescope. The main aim of this programme was to investigate the link between binarity and the presence of gravitationally bound material, and gain insight into the final evolution of what appears to be a significant population of binary stars.

We organised the paper as follows. In the next section we introduce the sample stars as well as the specific criteria used to select the objects discussed in this paper. In Sect. 3, we sketch the data gathering procedure as well as the reduction methods. In Sect. 4, we focus on the radial velocity determination, and in Sect. 5, we report on the analyses of the sample stars individually. In Sect. 6, we discuss the binary frequency of the sample and the analyses of the orbital elements. We then place our results in a broader context of stellar evolution.

2. Sample

The total sample selected by our specific criteria is described in detail in de Ruyter et al. (2006).

In this paper, we restricted ourselves to the stars in our radial velocity programme with spectral type F, five in total, which exhibit only small amplitude photometric variability with a peak-to-peak amplitude of up to 0.25 mag in the *V*-band and are accessible from the southern hemisphere. In addition, we included HD 131356 (EN TrA), which was recognised to be of RV Tauri type by Pel (1976) and found to have a large excess in L by Lloyd Evans (1985), despite the higher peak-to-peak pulsational amplitude. The main reason for its inclusion is that, because of the longer time baseline of our velocity monitoring, we were able to confirm the binary nature of the star and update the period estimate of Van Winckel et al. (1999). It shares the early F spectral type of the other stars discussed here, and in the 2001/2 season, its V amplitude was only 0.3 mag.

The spectral types are taken from objective prism work (Houk et al. 1976; MacConnell & Bidelman 1976; Kwok et al. 1997) in the case of IRAS 12222-4652 and EN TrA. The four remaining stars, which were all initially selected for their large infrared excesses (Lloyd Evans 1999), were classified by Lloyd Evans on the basis of blue light spectra of resolution 7 Å. Only the higher Balmer lines are relatively unaffected by emission. Intrinsic metal deficiency and subsequent depletion, weaken the metallic lines and vitiate the usual classification criteria. Luminosity class Ib was assumed to be broadly consistent with both the sharpness of the hydrogen lines and the similarity of the other properties of these stars to those of type II Cepheids. Published spectral types of B7III for IRAS 19125+0343 (Kwok et al. 1997) and B9Ib or B1III for IRAS 19157-0247 (Kwok et al. 1997; Parthasarathy et al. 2000; Gauba et al. 2003) may be discounted, since red spectra show strong lines of the CaII triplet,

Table 1. General characteristics of the sample.

IRAS	HD	sp. type	α_{2000}	δ_{2000}	l	b	m(v)	$T_{\rm eff}$(K)	log g	[Fe/H]	Reference
08544−4431	V390 Vel	F3	08 56 14.18	−44 43 10.7	265.51	+0.39	9.13	7250	1.5	−0.5	Maas et al. (2005)
12222−4652	HD 108015 NSV 5601	F3Ib	12 24 53.50	−47 09 07.5	298.25	+15.48	7.95	7000	1.5	−0.1	Van Winckel (1997)
14524−6838	HD 131356 EN TrA	F2Ib	14 57 00.69	−68 50 22.9	313.90	–8.68	8.77	6000	1.0	−0.7	Van Winckel (1997)
15469−5311		F3	15 50 43.80	−53 20 43.3	327.82	+0.63	10.56	7500	1.5	0.0	Maas et al. (2005)
19125+0343		F2	19 15 01.17	+03 48 42.7	39.02	–3.49	10.16	7750	1.0	−0.5	Maas et al. (2005)
19157−0247		F3	19 18 22.71	−02 42 10.8	33.59	–7.22	10.70	7750	1.0	−0.4	Maas et al. (2005)

Table 2. General characteristics of the spectral dataset obtained for every object.

Object IRAS	$N_{\rm tot}$	$N_{\rm used}$	ΔHJD (24+)	$\Delta V_{\rm rad}$ km s^{-1}	ΔV
08544−4431	181	161	51 147–54 487	22.1	0.25
12222−4652	83	82	45 397–53 833	13.5	0.23
14524−6838	75	63	48 313–53 904	45.7	0.81
15469−5311	175	161	51 278–54 680	28.2	0.25
19125+0343	103	90	51 278–54 331	29.6	0.19
19157−0247	137	111	51 279–54 680	24.2	0.23

which have an excited lower state and so do not appear as interstellar absorption lines, whereas the H and K lines of interstellar origin may be quite strong.

Cooler objects of the entire sample of de Ruyter et al. (2006) are in the Population II Cepheid instability strip and have photospheric pulsations of far larger amplitude. These stars have typical hydrogen line spectral types of G0 (Lloyd Evans 1999). In many of those, the pulsations show substantial cycle-to-cycle variability. These pulsations often show the defining alternating deep and shallow minima of RV Tauri stars. The detection of orbital motion in those objects is very difficult because of confusion with the radial velocity variations induced by the photospheric pulsations (Maas et al. 2002; Van Winckel et al. 1998, 1999).

In Table 1, the programme stars are listed with their spectral type, equatorial coordinates, Galactic coordinates, and visual mean magnitude. Mean photospheric characteristics are also given, including the appropriate reference.

3. Data and data reduction

In the framework of the cooperation between the Geneva Observatory and the Institute of Astronomy in Leuven (Belgium), the twin 1.2 m telescopes Euler (La Silla) and Mercator (La Palma) were constructed. Within this framework, the observers of Leuven have regular access to the Swiss Euler telescope operated by the Geneva observatory and the observers of the Geneva Observatory have regular access to the Flemish Mercator telescope operated by the Institute in Leuven. During the Leuven telescope time on Euler, typically 3 runs of 10−14 days every semester, the programme stars were monitored in radial velocity with the spectrograph CORALIE (Queloz et al. 1999). We started this campaign at the end of November 1998. In Table 2 we list the main characteristics of the observational data. $N_{\rm tot}$ is the number of observations, $N_{\rm used}$ the number used after our quality test (see later in the text), and ΔHJD is the time range of the observations. The total peak-to-peak radial velocity spread, $\Delta V_{\rm rad}$ (km s^{-1}) and ΔV, the visual photometric peak-to-peak variation, are also shown.

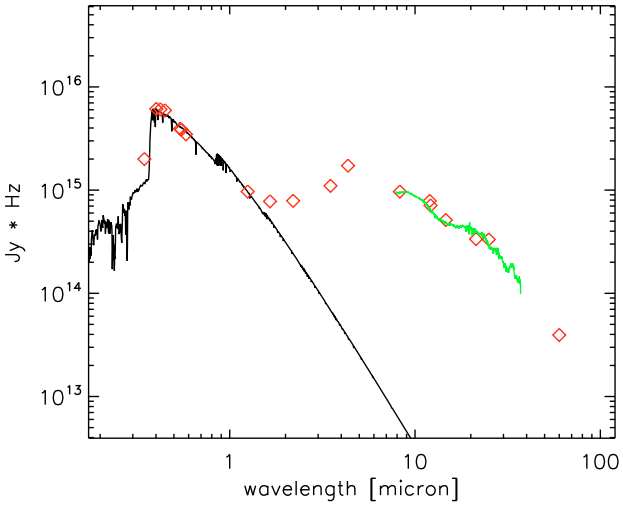

Fig. 1. The SED of IRAS 19125+0343. The SED is typical for the sample, showing a large and broad IR-excess. A total reddening of $E(B-V) = 1.1$ was deduced by minimizing the difference between the dereddened broadband fluxes (diamonds) and the appropriate model atmosphere (full black line). The infrared excess was not considered in this minimalisation. The Spitzer infrared spectrum (Gielen et al. 2008) is also shown.

The CORALIE spectrograph is a fibre-fed spectrograph that samples the visual spectrum in 68 spectral orders ranging from 388 nm to 682 nm. The resolving power ($\lambda/\Delta\lambda$) is 50 000 at 500 nm, with a 3 pixel sampling. The fibre diameter is 2 arcsec on the sky. We used the online data reduction system (Queloz et al. 1999), which includes all standard steps in echelle reduction.

Older radial velocity data of IRAS 12222-4652 and EN TrA are also included. These data were obtained with the CES spectrograph mounted on the CAT telescope at La Silla (ESO) as well as with the CORAVEL instrument mounted on the 1.5 m Danish telescope also on La Silla. CORAVEL is a spectrophotometer with which the radial velocity was obtained by cross-correlation of the stellar spectrum with a hardware mask created from the spectrum of the K2 III star Arcturus (Baranne et al. 1979). EN TrA has stronger lines than the other stars observed, so that clear correlation profiles are obtained from these data. The zeropoint of the system was regularly assessed during the night by measuring CORAVEL radial velocity standards. These calibrations were performed at intervals of about 1−2 h. All the CORAVEL observations, including ours, are held in a database that is maintained by the owners of the CORAVELs in Geneva.

The stars accessible from La Palma were included in the long-term photometric monitoring programme performed with the 1.2 m Mercator telescope using the refurbished Geneva 7-band dual-beam photometer (Raskin et al. 2004). This

Table 3. General characteristics of the photometric datasets obtained for every object.

Object	P7	SAAO	ASAS
IRAS 08544-4431		91 (50858–52060)	830 (51868–54843)
IRAS 12222-4652	120 (47258–47824)	166 (51625–53195)	576 (52441–54711)
EN TrA	61 (47608–49853)	58 (43979–49564)	633 (51905–54743)
IRAS 15469-5311		49 (48803–51712)	550 (51925–54743)
IRAS 19125+0343	47 (52415–53606)	30 (49485–51819)	362 (52442–54772)
IRAS 19157-0247	6 (52446–52561)	50 (48404–51819)	386 (51979–54777)

resulted in 47 high quality absolute photometric measurements for IRAS 19125+0343, but only 6 for IRAS 19157-0247. The seven bands are measured quasi-simultaneously using a filter wheel that cycles through all seven filters four times per second alternating as well between the sky and the object channel (Golay 1980). The same instrument was previously attached to the now decommissioned 0.7 m Swiss telescope at La Silla. During that period, we obtained many measurements for the Southern stars, IRAS 12222-4652 and EN TrA.

The photometric observations in the Cousins UBVRI system were obtained from SAAO with the Modular Photometer on the 0.5 m telescope and subsequently with a very similar photometer on the 0.75 m Automatic Photoelectric Telescope (Martinez et al. 2002). These observations were made with reference to the Cousins standards in the E-regions (Menzies et al. 1989). The data are contained in Table 5, except for EN TrA for which the observations were made by Berdnikov & Turner (1995) and Caldwell et al. (2001).

Since these monitoring programmes require the dedicated efforts of many people, the observers responsible for the data acquisition for this project are included as co-authors in alphabetical order.

We complemented our own observations with the V-band data available from the All Sky Automated Survey (Pojmanski 2002). These data were obtained with the ASAS-3 configuration using the wide field ($8.8^\circ \times 8.8^\circ$) CCD camera with a sampling of $\sim 15''$/pix. The critical PSF sampling is not reached and the pipeline reduction approximates aperture photometry with 5 circular apertures from 2 to 6 pixels in diameter. The ASAS guidelines foresee a preferred aperture for every magnitude bin and we limited our analysis to measurements with quality flag A, according to the less rigorous classification applied to the re-reduced data on the ASAS website. The recommended apertures were used, except that for IRAS 19125+0343 we used aperture 4, MAG-3, rather than aperture 1, MAG-2, to ensure full inclusion of the M star at an angular distance of 9.9 arcsec. We applied corrections for the small offsets between the magnitudes of the same star observed with different cameras and for the offsets between the original and later reductions of early observations, many of which were not included in the re-reduced data on the ASAS website after recovery from the data storage crash. The photometric zeropoint is tied to the Hipparcos catalogue, since in every frame a few hundred Hipparcos stars are located. These were used in the zeropoint definition (Pojmanski 2002). Near simultaneity of some of our observations with ASAS data enabled determination of zeropoint differences and error estimates. The offsets (ASAS-other), standard deviation (s.d.) of the single observations, the number of data points, and the source of comparison data are: IRAS 08544-4431, +0.043 mag, 0.010 mag, 14, SAAO; IRAS 12222-4652, +0.009, 0.015, 44, SAAO; IRAS 19125+0343, −0.057, 0.022, 18, P7; IRAS 19157-0247, +0.043, 0.023, 3, P7. These differences have been allowed for in combining the relevant datasets. Additionally, from non-overlapping datasets, we have offsets for IRAS 15469-5311, −0.030, SAAO; IRAS 19125+0343, +0.045, SAAO; IRAS 19157-0247, +0.070, SAAO. The SAAO magnitudes of IRAS 19125+0343 are 0.09 mag brighter than the P7 observations, because of the inclusion of the M star in the aperture used at SAAO. These last values will include any true changes in brightness between the two epochs.

The shift between SAAO and P7 for IRAS 19125+0343 is attributable to the inclusion or exclusion of the nearby M type star. The reason for offsets for other stars is unknown. The s.d. obtained by direct comparison of photometric data, are smaller than the errors ascribed to individual observations in ASAS, which must therefore be more precise than previously recognised. Intercomparison of three independent subsets within the ASAS data for IRAS 08544-4431 gives values in the range 0.011 to 0.024 mag, confirming the typical values above.

The ASAS data proved to be valuable in compensating for the poorer sampling of our own multi-colour measurements in the search for the long periods expected. ASAS data were used by Kiss et al. (2007) in their study of the pulsations of these and similar stars, but the continuation of the ASAS project has doubled the timespan of the observations, which now extend from 2001 or 2002 to the end of the 2008 season. Moreover, the re-reduction of much lost ASAS data has filled the gap around JD 2 453 500 seen in the plots by Kiss et al. (2007) for these stars. The more extensive data facilitate the characterisation of the noisy small amplitude oscillations of these stars.

In Table 3, we list the main characteristics of the raw photometric data sets for all objects. The number of measurements in the different photometric systems is given. P7 is the 7-band Geneva photometric system, SAAO is the Cousins UBVRI-system, and the ASAS monitoring is obtained in the V-band only. In brackets we show the total time coverage in HJD (24+).

4. Radial velocity determination

To obtain accurate radial velocity information based on low S/N spectra, we determined cross-correlation profiles for all individual measurements. The standard spectral mask includes a large set of distinctive spectral lines for the given spectral type. Our chemical analysis, based on high signal-to-noise optical spectra, showed that for most stars, several elements, including iron, are underabundant (Maas et al. 2005). By eliminating, from the standard spectral mask, those lines not detected in our high-quality spectrum, we created an appropriate spectral mask for every individual star. Moreover, we selected only single lines with clear symmetric profiles.

In Fig. 2, we compare the cross-correlation profile obtained by the standard mask with the one obtained by the specific mask, constructed on the basis of the high signal-to-noise ratio spectrum for IRAS 19157-0247. No accurate velocity can be derived by using the standard mask, while a Gaussian fit of the profile,

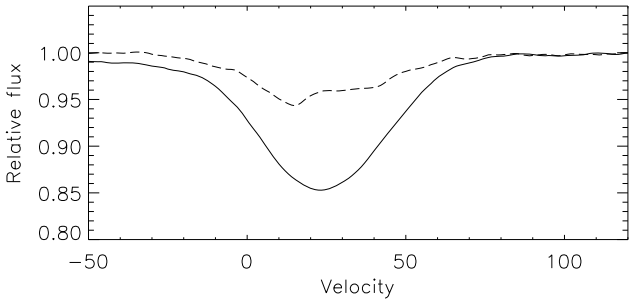

Fig. 2. Comparison between cross-correlation profiles obtained with a standard spectral mask (dashed line) and with a software mask adapted to the individual spectral characteristics of IRAS 19157-0247 (full line).

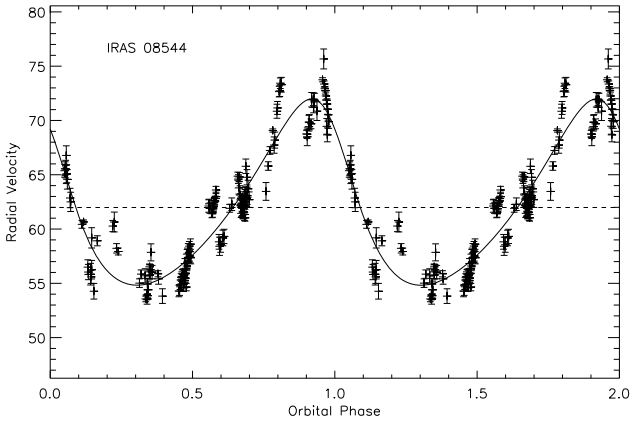

Fig. 3. The radial velocities folded on the orbital period of 508 days for IRAS 08544-4431. The errorbars are defined as the standard deviation in the 50-point bisector of the cross-correlation profile. The system velocity is given by a dashed line.

obtained by the specified mask for IRAS 19157-0247, provides a good estimate of the radial velocity.

The radial velocity is computed using the mean of a 50-point bisector of the cross-correlation function. An initial Gaussian fit was used to determine the bisector points, which are defined on an equidistant velocity grid centred on the velocity minimum of the Gaussian fit. The grid spans twice the Gaussian width (σ). The internal uncertainty in a radial velocity measurement is estimated from the rms of these 50 bisector values. We eliminated these cross-correlation profiles for which the rms is larger than 1 km s^{-1}. Several spectra were obtained in very poor weather conditions and/or guiding failures. These measurements were eliminated in this step of the analysis. Although the objects do not have a large pulsational amplitude, some objects do show asymmetries in these cross-correlation profiles at particular phases in the pulsation cycle. These profiles are also eliminated at this point bacause our study focuses on the detection of orbital motion. The number of radial velocity measurements that passed our critical quality assessment test is given in Table 2. The individual datapoints are given in Table 4.

5. Variability study of individual stars

The main goal of our programme was to search for evidence of binary motion in the radial velocity data and, if found, determine the orbital elements. Although for this paper, we selected objects with a small pulsational amplitude in V, they all show some photometric variability, which could also be present in the radial velocity data.

Luminous stars on the blue side of the population II Cepheid instability strip are, however, far from being regular monoperiodic pulsators and often exhibit a very complex pulsational behaviour. One example is HD 56126 (Barthès et al. 2000; Fokin et al. 2001), where the main pulsation mode is shown to generate shocks provoking a complex asynchronous motion in the outer layers. Another example is HR 7671 (HD 190390), where the main period of 28.6 days is accompanied by a beating behaviour caused either by a stable pulsation triplet or an unstable main period. Consequently, the description of the pulsation in radial velocity, modelled as a simple harmonic, fails to reproduce the complete dataset, which has a peak-to-peak difference of 8.2 km s^{-1}(Reyniers & Cuypers 2005), as well as a corresponding light amplitude of 0.36 mag. Neither object shows evidence of binary motion. Since the programme stars of this project are also on the hot side of the instability strip, we investigated the photometric dataset in parallel with the radial velocity data to compare radial velocity variability with photometric behaviour.

For the variability study, we used phase dispersion minimization PDM (Stellingwerf 1978) and, for the photometric data, the Lomb-Scargle method to search for periodicities. The orbital solutions were then computed using an altered version of the Fortran code VCURVE (Bertiau & Grobben 1969) as well as the minimisation code FOTEL (Hadrava 2004). The weights of the individual velocity points were based on the rms values of the bisector analyses. All errors quoted in the individual orbital elements are rms errors of these elements calculated from the covariance matrix. Plots of the photometry of single seasons were used to look at the individual cycles in some cases. The individual photometric datapoints are given in Tables 5 and 6.

5.1. IRAS 08544-4431

We demonstrated that this object is a spectroscopic binary in Maas et al. (2003). We continued our monitoring of this object to refine its orbital elements. We gathered a total of 161 good radial velocity measurements sampling more than 6 orbital periods. The resulting radial velocity variations are shown in Fig. 3. An orbital period of 508 days and an eccentricity of 0.25 were found. All orbital elements are listed in Table 7. In this table we list P as the orbital period in days, K as the velocity amplitude, e as the eccentricity, ω as the angle in the orbital plane between the direction to the ascending node and the direction to the periastron, T_0 as the time of periastron passage, γ as the system velocity, rms (O−C) as the root mean square of the errors, $a_1 \sin i$ as the semi major axis, $F(M)$ as the mass function in solar masses, N as the number of observations, Δt (cycles) as the number of cycles used and ΔV as the visual photometric peak-to-peak variation.

Our previous pulsational analysis of photometry from SAAO (Maas et al. 2003) showed that low-amplitude pulsations are present, but that the cycle-to-cycle variability is large. Periods of 72.3 and 89.9 d were reported. Kiss et al. (2007) confirmed the shorter period and obtained two new periods, 68.9 d and 133 d, from ASAS data that extended to JD 2 453 900, with a break 2 453 200−2 453 750.

We combined the SAAO and the highest quality ASAS dataset (see Table 3) and analysed the total V-band time-series. In Fig. 4, the total dataset is shown and a beating pattern with a clear amplitude modulation is present, as well as a slow brightening. The dominant period of 71.7 ± 0.4 d gives in a harmonic fit of 0.03 mag amplitude and a variance reduction of 21%.

Table 7. The orbital elements of the programme stars.

	IRAS 08544	σ	IRAS 12222	σ	EN Tra	σ	IRAS 15469	σ	IRAS 19125	σ	IRAS 19157	σ
Period (days)	507.8	1.5	913.8	4.3	1493.	7.	389.9	0.5	519.6	2	119.5	0.2
K (km s^{-1})	8.6	0.3	3.5	0.5	16.3	0.6	11.9	0.3	12.6	0.5	7.3	0.7
e	0.24	0.02	0.00	0.0	0.32	0.04	0.09	0.02	0.25	0.03	0.31	0.07
ω (°)	47.	7.			160.	6.	133.	16.	242.	6.	80.	14.
T_0 (periastron) (JD24+)	51482.	10.			538535.	22.	51491.	17	53061.	8.	51849.	5.
γ (km s^{-1})	61.98	0.16	3.65	0.17	−7.1	0.4	−14.9	0.2	67.0	0.3	33.1	0.3
rms (km s^{-1})	1.88		1.47		2.42		2.1		1.98		3.31	
$a_1 \sin i$ (AU)	0.39	0.01	0.29	0.04	2.12	0.08	0.42	0.01	0.58	0.02	0.08	0.01
$F(M)$ ($M_\odot$)	0.0304	0.0033	0.0042	0.0017	0.57	0.06	0.068	0.006	0.097	0.012	0.0041	0.0012
N	161		82		63		161		90		111	
Δt (cycles)	6.6		9.2		3.8		8.7		5.9		28.4	
$\Delta m(V)$	0.25		0.23		0.81		0.25		0.19		0.23	

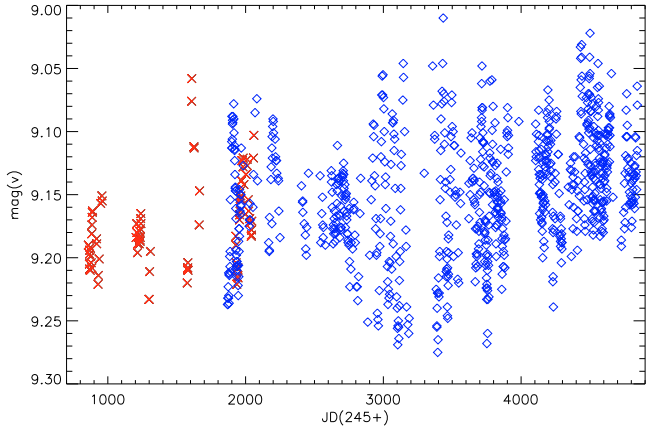

Fig. 4. The combined datasets of the V-band photometric measurements of IRAS 08544-4431. The x-symbols are the SAAO data and the diamonds are the ASAS measurements.

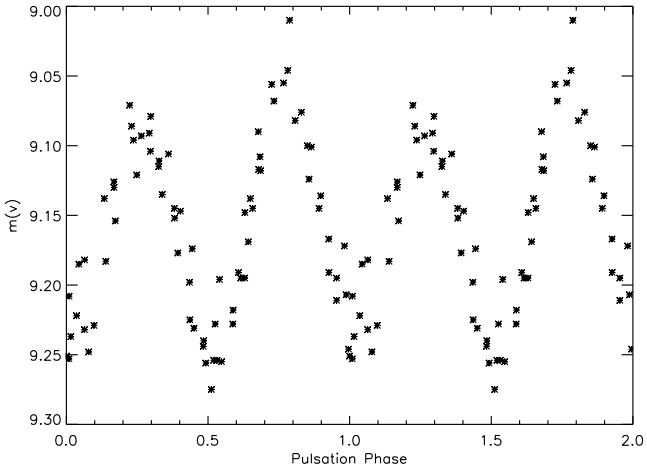

Fig. 5. The V magnitudes for IRAS 08544-4431 plotted against the double period, 143.6 days. Data of period JD 2 452 887−2 453 397, when IRAS 08544-4431 showed a large amplitude.

The amplitude was greatest, at 0.20 mag, during the interval from JD 2 452 850 to 2 453 500. Figure 5 shows these data, phased at the double period 143.6 d. The alternate minima are of different depth and the alternate maxima are of unequal height, although the differences are quite small. The behaviour was maintained for almost 2 years and is reminiscent of the typical RV Tauri light curves, albeit of a far smaller amplitude. Much of the small scatter may be attributed to the observational error of about 0.02 mag. Corresponding plots for the two intervals of small amplitude, represented by SAAO data from JD 2 450 850 to 2 451 500 and ASAS data from JD 2 452 400 to 2 452 750 show amplitudes of 0.08 mag and 0.06 mag, respectively, while the curves are less clearly defined. The separation of these intervals, at least 1400 d, is less than expected for a beat between the two principal periods, 2800 d, as suggested by Kiss et al. (2007), although the next interval of small amplitude had not occurred by early 2009, JD 2 454 840, and may yet fit the prediction.

There is evidence of this orbital period in neither the ASAS photometry (Kiss et al. 2007) nor our extended multicolour photometry. Given the complex atmospheric pulsations, we did not attempt to clean the low amplitude irregular pulsational variability from the radial velocity dataset.

5.2. IRAS 12222-4652

IRAS 12222-4652 also exhibits a complex pulsational pattern with a significant amplitude modulation and a smaller amplitude at earlier times (see Fig. 6). ASAS data for the period before JD 2 452 300 have been rejected as they were highly erratic, in contrast to contemporaneous SAAO data. Our Geneva photometry was poorly sampled over many years, while the SAAO and ASAS photometry combine well to provide a larger dataset. We find a dominant period of 60.5 ± 0.11 d and a second period of 55.3 ± 0.2 d, in agreement with (Kiss et al. 2007). A combined harmonic fit infers a fractional variance reduction of 52%. Plots of the V magnitude against time show continuous variability in the amplitudes and lengths of successive cycles, from 0.11 to 0.20 mag and from 48 to 76 days. The longer cycles tend to have amplitudes that are below average. The PDM analysis also yields an additional period of 120.6 ± 1.0 d, or twice the principal period. IRAS 12222-4652 is clearly another star with a complex dynamical photosphere, which complicates the interpretation of its radial velocity variations.

The total radial velocity dataset of IRAS 12222-4652 includes older data, measured on high-quality spectra obtained to study the chemical composition (Van Winckel 1997). Our total timespan is therefore longer than 23 years. The dataset infers a significant initial period of 917 ± 4 days, which we interpret as due to orbital motion. A circular orbit gives a fractional variance reduction of 65%. After cleaning this first circular model, we retrieve the dominant photometric period of 60.5 d in our θ-statistic with an amplitude of 1.4 km s^{-1}. Our final orbital solution (see Fig. 7) is then obtained after cleaning the original dataset with

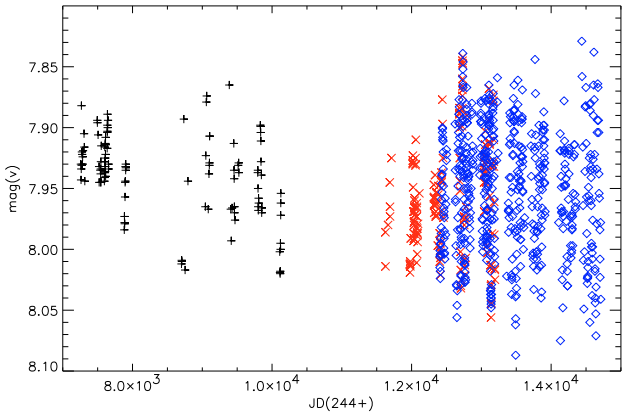

Fig. 6. The combined datasets of the V-band photometric measurements of IRAS 12222-4652. The + are the Geneva measurements, the x-symbols are the SAAO data and the diamonds are the ASAS measurements.

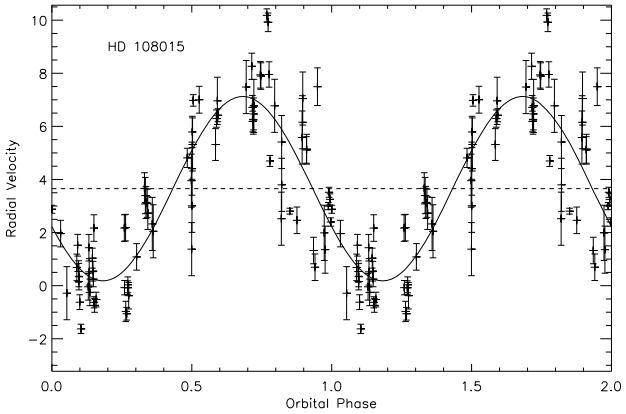

Fig. 7. The radial velocity variations of IRAS 12222-4652, after correction for the variations induced by the pulsations. The data are folded at the orbital period of 914 days. The full line is a circular model for the orbit.

the harmonic fit of the dominant photospheric pulsation mode. The small eccentricity does not differ significantly from zero, so our final solution gives a circular orbit of 914 ± 4 days. The fractional variance reduction is 75%. The orbital period is not present, either in magnitude or colours.

5.3. EN TrA

HD 131356 (EN TrA) was discovered to be variable by Miss Leavitt (Pickering 1907). The binary nature and preliminary orbital elements were given in Van Winckel et al. (1999). We have since accumulated more data using the CORALIE spectrograph to improve the orbital solution.

The object is catalogued in the GCVS as a small amplitude Cepheid with a published pulsation period of 36.54 d (Grayzeck 1978), based on a limited dataset covering part of two pulsational cycles, with poor coverage in phase. Pel (1976) obtained a continuous time-series of 44 measurements on the Walraven photometric system. The object showed at that time (JD 2 440 990−2 441 171) a large V-band amplitude with a maximum of $V = 8.55$, a deep minimum of 9.2, and a shallow minimum of 8.8. The Hipparcos catalogue (HIP 73152) lists a period of 37.10 days (Perryman & ESA 1997).

Our Geneva photometry is poorly sampled and no periodicity could be determined. Two sets of observations obtained at

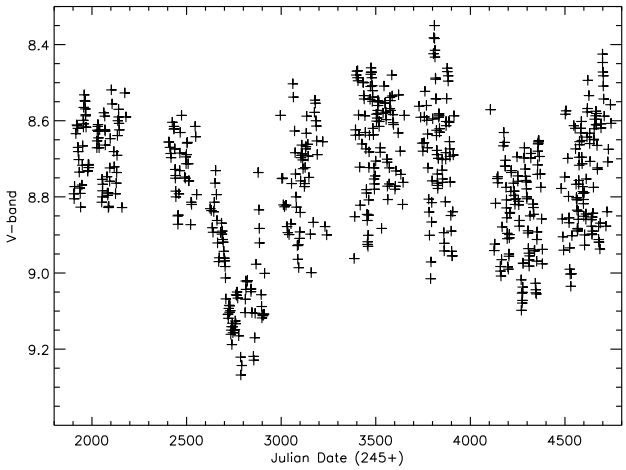

Fig. 8. The V-band photometric dataset of EN TrA obtained by the ASAS project (Pojmanski 2002).

SAAO on the UBVRI system are available, comprising 42 observations (JD 2 443 979−2 445 155) by Caldwell et al. (2001) and 16 observations (JD 2 449 522−2 449 564) by Berdnikov & Turner (1995). Both indicate a range of $V = 8.5$−9.05, with little difference between deep and shallow minima. A short dataset by Eggen (1986) gives a range of V-magnitudes between 8.55 and 8.96, without full coverage of the extrema. The first season of ASAS data, 2001−2002, shows a variable amplitude of up to 0.3 mag, similar to the other stars (see Fig. 10).

EN TrA fades by some 0.5 mag near JD 2 452 800 and again, by about 0.1 mag, near JD 2 454 300 (see Fig. 8). Outside the intervals, the mean magnitude is fairly constant but the amplitude is variable. A period analysis infers a single period $P = 37.04 \pm 0.03$ d and a double period 74.1 ± 0.1 d. Aliases correspond to the orbital period and the calendar year. The magnitudes at maximum and minimum light are both very variable from cycle to cycle and from year to year. The deep and shallow minima, and bright and faint maxima, generally retain the same relative phasing within a given season, but they sometimes interchange in successive years. These phenomena are well known in RV Tauri stars.

Because of the very long baseline of our radial velocity data, we could sample about 3.7 orbital cycles. In a first iteration, after the removal of the orbital solution, the residuals showed a very clear periodicity with a period of 36.70 d, which we link to the pulsation timescale found in the photometry. A harmonic fit inferred a radial velocity amplitude of 4 km s^{-1} and we cleaned the original data with this mean pulsation model. The final solution gives an orbit with a period of 1493 ± 10 days and a large eccentricity of 0.31 ± 0.05. (see Fig. 9, Table 7).

To investigate the secular variations in the mean magnitude, we selected only those pulsation cycles for which 6 or more data points are available. We then cleaned the pulsation amplitude and reduced the pulsation cycle to the mean magnitude alone. This mean magnitude is around 8.6, but there is a significant drop when the object enters the conjunction phase (see Fig. 9). The minimum (mean magnitude of 9.1) is obtained at exactly inferior conjunction and EN TrA then slowly recovers to its nominal mean values of about 0.3 in orbital phase later. There are shallower fadings at the same orbital phase: three orbits earlier, near JD 2 448 350 (P7 data) and JD 2 454 300 (ASAS data). The corresponding orbital phase is not covered by any of the other datasets. The most natural explanation of the secular variability is that the star experiences from variable circumstellar reddening

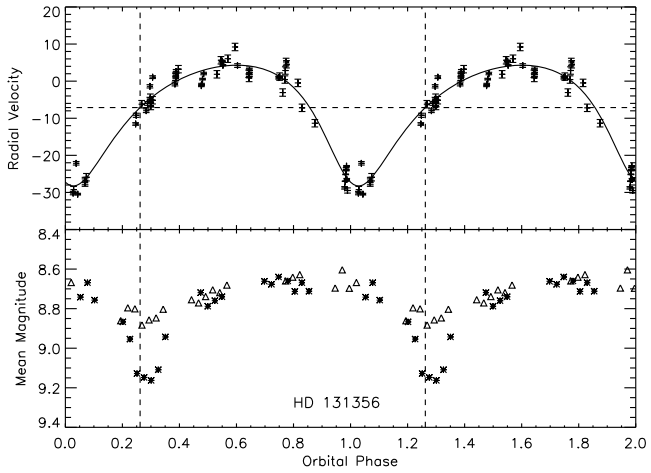

Fig. 9. *The top panel* shows the radial velocity variations of EN TrA folded at the orbital period of 1493 days. The full line represents the orbital model. *The lower panel* gives the mean magnitude determined on those pulsation cycles with more than six data points. The different symbols represent two different orbital cycles. Mean minimal light is measured when the object is at inferior conjunction but in the two different orbital cycles, the effect is not equally prominent.

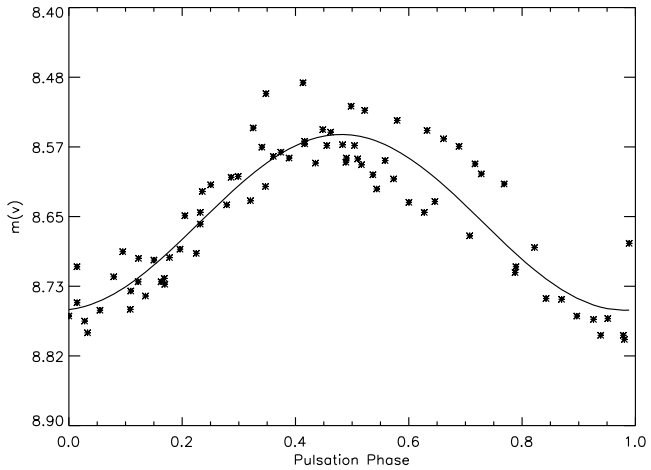

Fig. 10. The V-band magnitudes of EN TrA, from the ASAS photometric monitoring project of the first season (JD 2 451 903−2 452 173), folded on the pulsation period of 36.70 days found in the radial velocity data.

during orbital motion. The minimum is reached when the object suffers from a maximal reddening of circumstellar material in the line-of-sight, which would occur when the star is at inferior conjunction if there is a circumbinary disk.

5.4. IRAS 15469-5311

IRAS 15469-5311 is another low-amplitude pulsator that has been little studied in the literature. The mean magnitude varies with a fairly abrupt brightening of 0.045 mag after JD 2 454 000, and exhibits smaller variations on a timescale greater than 1000 days. We combined the ASAS and SAAO photometric V-band measurements for the pulsation study. The main period is 54.5 ± 0.3 d, which is consistent with that of 54.4 ± 1 d found by Kiss et al. (2007), and a harmonic fit gives a fractional variance reduction of 21% with an amplitude of only 0.028 mag. The extended dataset did not confirm the second pulsation period of 49.1 days given by Kiss et al. (2007); this might be a one

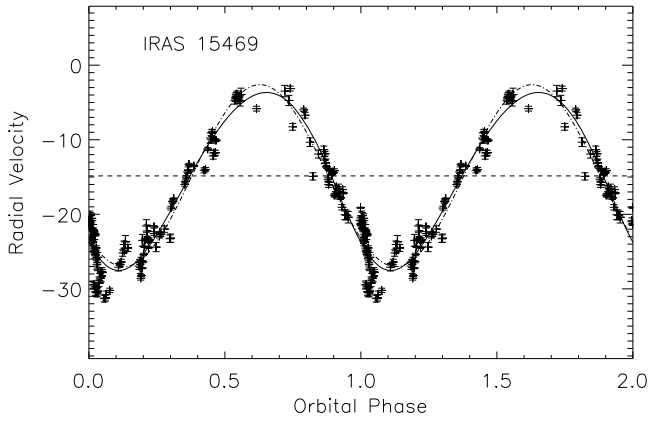

Fig. 11. The radial velocities of IRAS 15469-5311 folded ot the orbital period of 389.9 days. The full line is the orbital solution, and the dash-dotted line is the best-fit circular orbital curve.

year alias of the primary period. The cleaned data yield the next possible period of 56.6 ± 0.3 d, but the variance reduction is limited. Possible other periods of 164 and 77 days may be spurious as well, as they also appear in the windowed data. Plots of magnitude against JD for 20 well observed cycles in four seasons give lengths of 32 to 77 days, with a mean of 54.0 days. The amplitude varies from 0.02 mag to 0.15 mag. The mean amplitude quoted above is an underestimate of the true variability, as the mean light curve is blurred by variability in both amplitude and length of period. The double period also emerges from the PDM analysis and a plot of V against 109.2 days shows a weak tendency towards alternate deep and shallow minima, as well as bright and faint maxima.

We have 160 good radial velocity measurements for IRAS 15469-5311 over a time range of 3402 days. The orbit of 390 days is very well defined (see Fig. 11). The classical Lucy and Sweeney test (Lucy & Sweeney 1971) shows that the orbit has a small but significant eccentricity of 0.09. In Table 7, all other orbital parameters are given. There is an indication of the orbital period in the photometric data, for which Kiss et al. (2007) give a period of 384 ± 50 days, but the phase diagram is not convincing. The residual velocity variations have a peak-to-peak amplitude of 10 km s^{-1} (standard deviation of 2.1 km s^{-1}), but there is no clear indication of the main pulsation period nor could we discover a clear periodicity in the residuals.

5.5. IRAS 19125+0343

IRAS 19125+0343 is also a poorly studied object, despite having both rather bright IRAS fluxes and a significant visual flux of $m(v)$ = 10.16. The LRS-IRAS spectrum is featureless (Kwok et al. 1997) and the source was not detected in the OH survey of Le Squeren et al. (1992). The object was rediscovered by Lloyd Evans (1999) in the search for new RV Tauri stars.

The photometric variability is small: the SAAO and P7 datasets give ranges of 0.11 and 0.07 mag, respectively, in the V-band. Kiss et al. (2007) found a possible long period of 2300 d; the more extensive ASAS data available now are consistent with this, with an amplitude of about 0.03 mag, but instead a step change of 0.03 mag fainter after JD 2 453 400 is a possibility.

Application of the period search algorithms to the complete dataset yielded several periods between 34 and 43 days, 42.3 and 38.9 days being the strongest. Phase plots against any of these periods showed much greater scatter than can be attributed

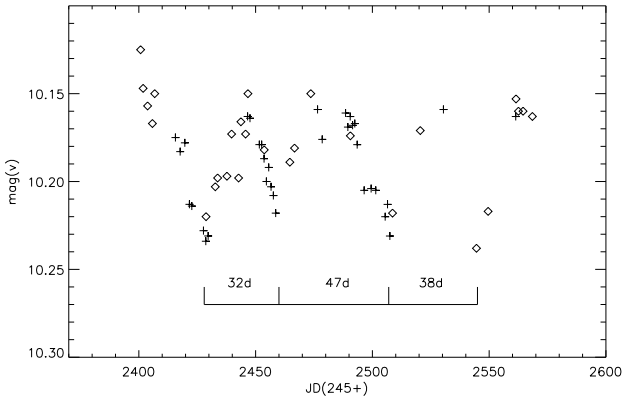

Fig. 12. Detail of the lightcurve of IRAS 19125+0343. Period changes occur on irregular time intervals illustrating the strong cycle-to-cycle differences observed in this object. P7 data are denoted by plus signs and ASAS data by diamonds.

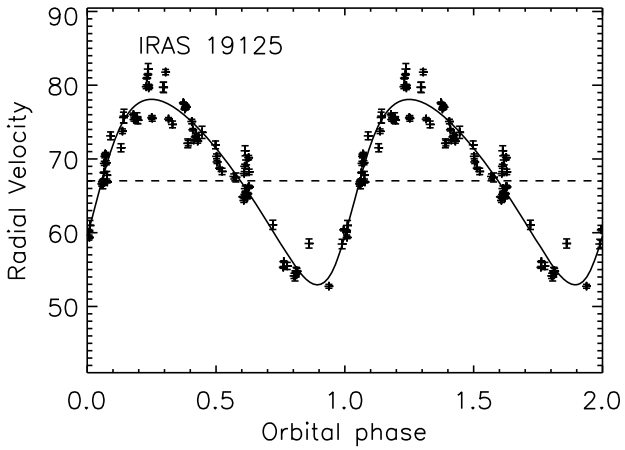

Fig. 13. The radial velocity data are folded at the orbital period of IRAS 19125+0343, 519.6 days. The full line is the orbital model.

to observational errors. The light curves (Fig. 12) for individual seasons were inspected, and the times between identifiable features, generally near the mean magnitude on the ascending or declining branches of the light curve, were estimated for successive cycles. There were insufficient data in 2006, and variations were small and/or erratic in 2004, 2005, and 2007. Estimates of the period could be made for 1994, from SAAO data, for 2002, from P7 and ASAS data, and for 2003 and 2008 from ASAS data. The values for 15 cycles ranged from 29 to 51 days, with a mean of 38.2 days. On two occasions, an incipient decline after maximum was reversed to give a second maximum and an unusually long interval between mid-decline points. This occurred in 2002, turning a tentative 32 day interval into 47 days, and in 2003, turning a 39 day interval into 51 days. The 519 d orbital period is not present in the photometry.

We have 91 good radial velocity measurements over a time range of 3389 days. We found a clear periodicity of 519 days and the peak-to-peak velocity amplitude is no less than 29.5 km s^{-1}. Given the period and amplitude, we interpret this variability as being due to orbital motion. We obtained orbital elements with a significant eccentricity of 0.26 ± 0.03. We sampled in total 6.5 orbital cycles. Figure 13 shows the radial velocities folded on this period. The full line represents the best-fit Keplerian orbital solution (see Table 7).

The strongest peak in both the PDM and Scargle periodograms for the residual velocity variations corresponds to 43 days, which leads to a variance reduction of 39%, and is fairly close to the mean of the cycle lengths found in the photometry. The orbital period is much shorter than the possible long photometric period (Kiss et al. 2007) in the ASAS data.

5.6. IRAS 19157-0247

The SAAO and ASAS photometry show that IRAS 19157-0247 varies with an amplitude of up to 0.15 mag but there is no long-term trend, although there is a possible modulation in the amplitude. The ASAS photometry, whether taken as a whole or subdivided into shorter intervals, or supplemented by the SAAO and P7 data, consistently indicates periods of 22.5 to 22.8 days, but with low significance. This period does not give a satisfactory light curve for any of these datasets, even for the data obtained in a single season: there is only a weak tendency toward a variation with phase in the derived period. Detailed examination of the time series for individual seasons shows great variability in both amplitude and length of successive cycles. The data are undersampled for this star, making delineation of the variability difficult. Kiss et al. (2007) found an irregular variation, with a possible periodicity of 25 days.

We have 111 radial velocity measurements over a time range of 3397 days. Both PDM and a Fourier analysis indicate that the 120 day period is significant. This period in radial velocity is not present in the photometry and we interpret this as the orbital period. The non-pulsational origin of the 120 day period is corroborated by two arguments. First, 120 days is a very long pulsational period for an F-type post-AGB star, and in any case it is not found in the photometric analysis. Secondly, the peak-to-peak variations in V for IRAS 19157-0247 average 0.13 mag at most, so it is very doubtful that the radial velocity variations with a peak-to-peak amplitude of 24 km s^{-1} are only due to pulsations. Interpreting the velocity curve as being produced by pulsations of the photosphere, the integrated velocity would yield a radius increase of about half the initial radius. Such a pulsation would clearly not go unnoticed in the photometry. We therefore interpret the velocity variations as being caused by orbital motion. This is a very short orbital period with a high eccentricity placing strong constraints on the evolutionary history of the star!

Figure 14 shows the radial velocities and the residuals folded at this period. We found an eccentricity of 0.31. The other orbital elements are shown in Table 7. The non-zero eccentricity was tested with the classical Lucy and Sweeney test (Lucy & Sweeney 1971). The value of $\sum(O-C)^2$ is 14% higher for a circular fit. This, together with the many cycles sampled, shows that the eccentricity is significant. The periodograms for the residual velocities show several peaks between 9 and 20 days, probably related to the timescale of the pulsations. None of them, however, lead to a significant variance reduction.

6. Discussion

6.1. Orbits

The most important conclusion of this extensive monitoring effort is that we have proven that all the stars in the programme are binaries. Unsurprisingly, given the high luminosities of the primaries, they are single-lined spectroscopic binaries because we have found no evidence in the spectra of flux contributions from a companion.

The orbital elements cover a wide range of periods, from 120 to 1500 days, for a range in mass functions of 0.004 to 0.57 $M_{\odot}$.

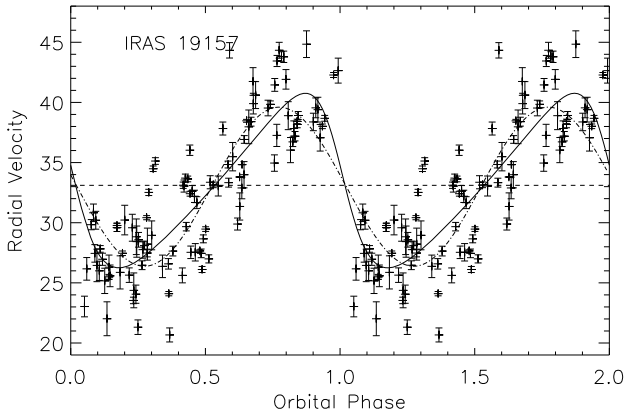

Fig. 14. The radial velocities of IRAS 19157-0247 folded at the orbital period of 119.5 days. The full line is the best-fit orbital model, the dashed-dotted line is the circular model. The horizontal line indicates the system velocity.

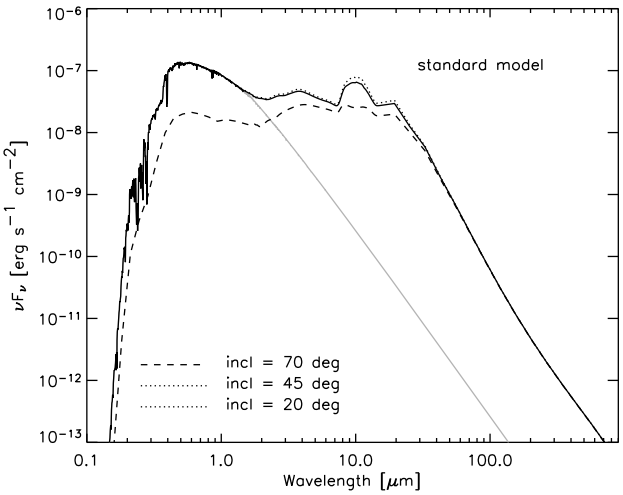

Fig. 15. The impact of the inclination on the SED computed by radiative transfer using typical parameters for a passively irradiated disc. The lower inclinations coincide on this scale so the same dotted line is used.

Table 8. The evaluation of the mass of the invisible companion of every programme star.

Star	Mass of the companion in solar mass.	
	$i = 90°$	$i = 65°$
IRAS 08544-4431	0.29	0.33
IRAS 12222-4652	0.13	0.15
EN TrA	1.25	1.50
IRAS 15469-5311	0.41	0.47
IRAS 19125+0343	0.49	0.56
IRAS 19157-0247	0.13	0.15

The semi-major axes of the orbits of the primaries around the centre of mass cover the range $a \sin i = 0.08$ to 2.1 AU. These are rather small orbits compared to the dimensions of a single AGB star. With their present estimated luminosity, these stars were too large while on the AGB to fit within their orbits and they must have been subject to severe binary interaction.

The physical interpretation of the orbital elements is hampered by the unknown inclination. Provided the evolved component has a remaining canonical mass of 0.6 $M_\odot$, the minimal masses of the companions are given in Table 8 as well as the masses obtained assuming an inclination of 65°.

It is, however, very unlikely that we observe the objects nearly edge-on. To quantify the impact of the inclination on the observed SED and observed line-of-sight reddening, we used the detailed radiative transfer model of the disc around IRAS 08544-4431 (Deroo et al. 2007) and assumed that a similar model applies to all programme stars. The inner hole is dust free since we assume that dust grains cannot exist above the sublimation temperature. The presence of this inner gap allows the existence of a vertical boundary directly irradiated by the central star, creating a puffed-up geometry (Deroo et al. 2007). The scale height of the disc must be significant in all objects because of the very significant near infrared luminosity in the entire sample (de Ruyter et al. 2006). The temperature, density, and scale height of the disc are calculated based on the condition of hydrostatic equilibrium, and iterated to obtain the convergent structure. The constraints on the model parameters of the disc around IRAS 08544-4431 were taken from spectrally resolved interferometric data in both the near-IR and the N-band (Deroo et al. 2007).

In Fig. 15, we show the impact of different inclinations on the SED. The figure illustrates that around an inclination of 70°, the line-of-sight towards the central object will graze the disc. This will strongly affect the circumstellar reddening. The line-of-sight circumstellar reddening in the 70° model is about $E(B-V) = 0.8$. Edge-on, the discs are strongly opaque and no direct visible light of the central star will reach us. The objects with the largest reddening are IRAS 08544-4431, IRAS 15469-5311, and IRAS 19125+0343 with $E(B-V) = 1.5 \pm 0.3$, 1.5 ± 0.3, and 1.2 ± 0.3, respectively (de Ruyter et al. 2006). The low Galactic latitudes and the strong interstellar DIBs in their spectra (Fig. 3 of Maas et al. 2005) indicate, however, that the greater part is of interstellar origin. We conclude that in all six objects, the inclination of the orbit is very likely to be less than or equal to 65° and the corresponding lower limits to the mass estimates are also given in Table 8. EN TrA is the only object for which we have direct evidence that the companion is too massive to be a white dwarf. We also note that for the other objects, there is no evidence of a hot white dwarf, in neither the energetics nor the lack of spectroscopic evidence of symbiotic activity. The companion stars are likely to be unevolved main-sequence stars, which do not contribute significantly to the energy budget of the systems.

6.2. Chemical composition

A surprising effect of the presence of a disc is that the photospheric chemical content can be strongly affected by depletion (Van Winckel et al. 1992; Waters et al. 1992). The observed chemical pattern in the photospheres is the result of gas-dust separation followed by re-accretion of only the gas, which is poor in refractory elements. The photospheres are then deficient in refractories (such as Fe and Ca and the s-process elements), while the non-refractories are not affected. Photospheric depletion is surprisingly common in evolved objects (Giridhar et al. 2005; Maas et al. 2005, 2007, and references therein). We also found that depletion is present in the LMC (Reyniers & van Winckel 2007), again around objects where the presence of a gravitationally bound disc is suspected.

Here we strengthen the link between the efficiency of the depletion process and the binary nature of the object. IRAS 08544-4431, IRAS 15469-5311, IRAS 19125+0343, and, to a much lesser extent, IRAS 19157-0247 are affected by photospheric depletion (Maas et al. 2005). EN TrA is iron deficient but the signature of depletion is less clear, while IRAS 12222-4652

has mainly solar abundances (Van Winckel 1997). The depletion process will mask third dredge-up chemical enrichment since the s-process elements are strongly refractory (Lodders 2003). In none of these objects is there any evidence of AGB nucleosynthetic enrichment.

Infrared spectra of EN TrA, IRAS 19125+0343, and IRAS 19157-0247 were presented by Gielen et al. (2008), and for IRAS 08544-4431 by Deroo et al. (2007). In all objects, the dust features are dominated by silicates and characterised by a very strong degree of processing both in grainsize and crystallinity. The dust disc creation occurred when the envelope was O-rich. This is a general characteristic of the entire sample (Van Winckel 2003) and the chemical evidence of both the photospheres and the circumstellar material show that the AGB evolution of those binaries was cut short by the phase of strong binary interaction.

6.3. Binary evolution

Calculations from Schuerman (1972) show that, when one takes into account the radiation pressure of the AGB-star in a close binary system, the critical Roche potential degenerates into a surface containing the inner Lagrangian point L_1 and the outer Lagrangian point L_2 for a critical ratio of the radiation pressure force to the gravitational attraction. For this critical ratio, material lost by the AGB star flows through the L_1 point and can settle itself through the L_2 point into a circumbinary disc (see also Frankowski & Jorissen 2007).

Population synthesis experiments (Bonačić Marinović et al. 2008) account for tidally enhanced mass-loss (Tout & Eggleton 1988) during AGB evolution and balance the eccentricity pumping mechanisms induced by a prescription of the mass-loss that is orbital phase related, so that at periastron passage, mass loss is enhanced (Soker 2000). The conclusion of Bonačić Marinović et al. (2008) was that the eccentricity enhancement process is in balance with the circularisation for objects that do not enter the common envelope phase and are expected to leave the AGB in orbits of around 1000 days or longer. The eccentric orbits with shorter periods (those of IRAS 08544-4431, IRAS 15469-5311, IRAS 19125+0343, and especially IRAS 19157-0247) are still not accounted for. In these systems, additional eccentricity pumping mechanisms should be at work which may be linked to the presence of the circumbinary disc (Waelkens et al. 1996; Artymowicz et al. 1991). Similar but less pronounced excess eccentricities with respect to theory are found in related objects (e.g., Jorissen et al. 2009). Despite the phase of strong binary interaction, there is no evidence that the mass transfer towards the undetected companion has been very efficient, the mass functions implying rather low minimal masses for the secondary (see Table 8).

The global picture that emerges from our radial velocity monitoring is that the post-AGB stars evolved in a system that is too small to accommodate a peak AGB star. During a poorly understood phase of strong interaction, which for small orbits was probably a common envelope phase, a circumbinary dusty disc was formed, but the binary system did not experience a dramatic decrease in orbital radius. What we observe now is an F-G supergiant in a binary system, which is surrounded by a circumbinary dusty disc in a bound orbit. Although not yet proven, the fact that we found a 100% binarity rate for our subsample of objects with low pulsational amplitude strongly favours the binary nature of all post-AGB stars with a hot dust component.

The formation, structure, and evolution of the disc are far from being understood, but do appear to be key ingredients in our understanding of the late evolution of a very significant binary population.

6.4. Variability

These six stars exhibit a wide range of properties, in particular in terms of amplitude and, especially, the regularity of variation. The first three stars, IRAS 08544-4431, IRAS 12222-4652, and EN TrA, have periodograms with peaks which stand out strongly from the noise, while IRAS 15469-5311 has a much weaker peak and IRAS 19125+0343 and IRAS 19157-0247 exhibit only a confused scatter, with minor peaks on a noisy background. IRAS 08544-4431 is the only one of the six stars to exhibit clearly defined, coherent variations for as long as one or two years. IRAS 12222-4652 and EN TrA have better defined peaks in their periodogram than IRAS 08544-4431, with a single period in the case of EN TrA, but their amplitudes and, in the case of IRAS 12222-4652, the lengths of individual cycles change continuously. The variations of IRAS 15469-5311 and IRAS 19125+0343 exhibit cycles of very variable amplitude and length, with evidence of changes in the direction of pulsation within a given cycle for IRAS 19125+0343, while the data for IRAS 19157-0247 are inadequate to elucidate the nature of the variations, which are probably even more irregular and of relatively short period.

These stars are of earlier spectral type and so are hotter than classical RV Tauri stars (Lloyd Evans 1999) and appear therefore to lie toward the blue side of the Cepheid instability strip. This raises a question about the nature of their pulsation. The ratio of the two principal periods is 0.96 for IRAS 08544-4431 and 0.91 for IRAS 12222-4652, whereas the ratio of the first overtone to the fundamental, P1/P0, is always close to 0.705 in classical Cepheids (Stobie 1977). Two high overtones might have the period ratios that we observe, but it seems implausible that these would be dominant, and the periods of these two stars are quite long, implying very long fundamental periods and a correspondingly high luminosity. This suggests that the pulsations of these stars are non-radial. EN TrA, which has a single, shorter, period and a larger amplitude, is, however, probably a radial pulsator. The apparently abrupt turnaround in the direction of the change in V magnitude, leading to a second maximum and a consequent lengthening of individual cycles in IRAS 19125+0343, recalls the suggestion that shockwaves may be involved in the complex motions of the outer atmosphere of the post-AGB star HD 56126 (Barthès et al. 2000).

The four stars of largest amplitude showed indications of the classical RV Tauri feature of alternating deep and shallow minima, but an equally large alternation of the magnitude at successive maxima.

Multicolour observations may be used to compare light and colour curves, which follow a similar phase relationship in classical Cepheids but which differ in type II Cepheids, for which an atmospheric shock leads to a bluer colour on the rise to maximum light, with wide loops in two-colour diagrams, whereas classical Cepheids have very narrow loops. The amount by which the B curve leads the V curve, in terms of relative phase in the single period, is: IRAS 08544-4431, 0.00:, IRAS 12222-4652, 0.04, EN TrA, 0.17. The scatter in the data and small amplitudes preclude any finding for the remaining stars. It is unfortunate that the SAAO observations of IRAS 08544-4431 were made when the amplitude was relatively small. It is only for EN TrA, the star of largest amplitude, that the phase shift typical of type II Cepheids is clearly seen.

7. Conclusions

The summary of the main conclusions of this contribution is that:

- Our radial velocity monitoring show that post-AGB stars that have both a hot dust component (and hence a disc) and a low photospheric pulsational amplitude (de Ruyter et al. 2006), are binaries. Even in these objects, the amplitude of the radial velocity variations induced by the pulsation is a significant fraction of the orbital velocity. It is an observational challenge to prove the binary nature of all post-AGB objects with a hot dust component, because in many systems large amplitude pulsations are present. Nevertheless, that 100% of our low amplitude pulsator programme stars are binaries is a strong indication that binarity is a prerequisite for disc formation.
- We confirm and strengthen the conclusion of Kiss et al. (2007) that complex multi-periodic but low-amplitude pulsational behaviour is present at the blue side of the type II Cepheid instability strip.
- The evolution of the binaries in the resulting period-eccentricity parameter space is not understood by using standard binary evolution channels. Theoretical efforts have included enhanced mass-loss and an efficient eccentricity pumping mechanism induced by modulation of the mass-loss in the orbital period. Nevertheless, the high eccentricity of IRAS 08544-4431, IRAS 19125+0343 and especially IRAS 19157-0247 (with a period of 120 days and a significant non-zero eccentricity) are detected in systems that are very likely to be post-common envelope systems and in these systems, the high eccentricity remains very poorly understood. The (on average) small mass functions imply that mass transfer to the companion has been limited.
- In all systems found so far, the dust in the disc is O-rich. The AGB evolution was likely cut short by the binary interaction event and with the orbital elements found in this work, the systems should be seen as post-interacting binaries rather than canonical post-AGB stars.
- The wide range of orbits and mass function detected here show that the creation of a circumbinary gravitationally bound disc is the final evolutionary product of a wide range of binaries.

Acknowledgements. The authors want to acknowledge the Geneva Observatory and its staff for the generous time allocation on the Swiss Euler telescope. The IvS acknowledges support from the Fund for Scientific Research of Flanders (FWO) under the grants G.0178.02., G.0703.08, G.0332.06 and G.0470.07. This research was made possible thanks to support from the Research Council of K.U.Leuven under grant GOA/2008/04. We would like to express our appreciation to Grzegorz Pojmanski for his efforts to provide and maintain the ASAS data in a form accessible to the astronomical community.

References

Artymowicz, P., Clarke, C. J., Lubow, S. H., & Pringle, J. E. 1991, ApJ, 370, L35
Balick, B., & Frank, A. 2002, ARA&A, 40, 439
Baranne, A., Mayor, M., & Poncet, J. L. 1979, Vistas Astron., 23, 279
Barthès, D., Lèbre, A., Gillet, D., & Mauron, N. 2000, A&A, 359, 168
Berdnikov, L. N., & Turner, D. G. 1995, Pis'ma Astronomich. Zh., 21, 603
Bertiau, F. C., & Grobben, J. 1969, Ricerche Astron., 8, 1
Bonačić Marinović, A. A., Glebbeek, E., & Pols, O. R. 2008, A&A, 480, 797
Bujarrabal, V., Castro-Carrizo, A., Alcolea, J., & Neri, R. 2005, A&A, 441, 1031
Caldwell, J. A. R., Coulson, I. M., Dean, J. F., & Berdnikov, L. N. 2001, J. Astron. Data, 7, 4
Cohen, M., Van Winckel, H., Bond, H. E., & Gull, T. R. 2004, AJ, 127, 2362
De Ruyter, S., Van Winckel, H., Dominik, C., Waters, L. B. F. M., & Dejonghe, H. 2005, A&A, 435, 161
de Ruyter, S., van Winckel, H., Maas, T., et al. 2006, A&A, 448, 641
Deroo, P., van Winckel, H., Min, M., et al. 2006, A&A, 450, 181
Deroo, P., Acke, B., Verhoelst, T., et al. 2007, A&A, 474, L45
Eggen, O. J. 1986, AJ, 91, 890
Fokin, A. B., Lèbre, A., Le Coroller, H., & Gillet, D. 2001, A&A, 378, 546
Frankowski, A., & Jorissen, A. 2007, Baltic Astron., 16, 104
Gauba, G., Parthasarathy, M., Kumar, B., Yadav, R. K. S., & Sagar, R. 2003, A&A, 404, 305
Gielen, C., van Winckel, H., Waters, L. B. F. M., Min, M., & Dominik, C. 2007, A&A, 475, 629
Gielen, C., van Winckel, H., Min, M., Waters, L. B. F. M., & Lloyd Evans, T. 2008, A&A, 490, 725
Giridhar, S., Lambert, D. L., Reddy, B. E., Gonzalez, G., & Yong, D. 2005, ApJ, 627, 432
Golay, M. 1980, Vistas Astron., 24, 141
Grayzeck, E. J. 1978, AJ, 83, 1397
Hadrava, P. 2004, Publ. Astron. Inst. Czechoslovak Acad. Sci., 92, 1
Houk, N., Hartoog, M. R., & Cowley, A. P. 1976, AJ, 81, 116
Jorissen, A., Frankowski, A., Famaey, B., & Van Eck, S. 2009, arXiv e-prints
Kiss, L. L., Derekas, A., Szabó, G. M., Bedding, T. R., & Szabados, L. 2007, MNRAS, 375, 1338
Kwok, S., Volk, K., & Bidelman, W. P. 1997, ApJS, 112, 557
Le Squeren, A. M., Sivagnanam, P., Dennefeld, M., & David, P. 1992, A&A, 254, 133
Lloyd Evans, T. 1985, MNRAS, 217, 493
Lloyd Evans, T. 1999, in Asymptotic Giant Branch Stars, IAU Symp., 191, 453
Lodders, K. 2003, ApJ, 591, 1220
Lucy, L. B., & Sweeney, M. A. 1971, AJ, 76, 544
Maas, T., Van Winckel, H., & Waelkens, C. 2002, A&A, 386, 504
Maas, T., Van Winckel, H., Lloyd Evans, T., et al. 2003, A&A, 405, 271
Maas, T., Van Winckel, H., & Lloyd Evans, T. 2005, A&A, 429, 297
Maas, T., Giridhar, S., & Lambert, D. L. 2007, ApJ, 666, 378
MacConnell, D. J., & Bidelman, W. P. 1976, AJ, 81, 225
Martinez, P., Kilkenny, D. M., Cox, G., et al. 2002, Monthly Notes of the Astronomical Society of South Africa, 61, 102
Men'shchikov, A. B., Schertl, D., Tuthill, P. G., Weigelt, G., & Yungelson, L. R. 2002, A&A, 393, 867
Menzies, J. W., Cousins, A. W. J., Banfield, R. M., & Laing, J. D. 1989, South African Astronomical Observatory Circ., 13, 1
Miszalski, B., Acker, A., Moffat, A. F. J., Parker, Q. A., & Udalski, A. 2009, A&A, 496, 813
Moe, M., & De Marco, O. 2006, ApJ, 650, 916
Parthasarathy, M., Vijapurkar, J., & Drilling, J. S. 2000, A&AS, 145, 269
Pel, J. W. 1976, A&AS, 24, 413
Perryman, M. A. C., & ESA 1997, The HIPPARCOS and TYCHO catalogues. Astrometric and photometric star catalogues derived from the ESA HIPPARCOS Space Astrometry Mission, ESA SP, 1200
Pickering, E. C. 1907, Astron. Nachr., 175, 333
Pojmanski, G. 2002, Acta Astron., 52, 397
Queloz, D., Casse, M., & Mayor, M. 1999, in Precise Stellar Radial Velocities, ed. J. B. Hearnshaw, & C. D. Scarfe, IAU Colloq., 170, ASP Conf. Ser., 185, 13
Raskin, G., Burki, G., Burnet, M., et al. 2004, in SPIE Conf. Ser., 5492, 830
Reyniers, M., & Cuypers, J. 2005, A&A, 432, 595
Reyniers, M., & van Winckel, H. 2007, A&A, 463, L1
Sahai, R., Morris, M., Sánchez Contreras, C., & Claussen, M. 2007, AJ, 134, 2200
Schuerman, D. W. 1972, Ap&SS, 19, 351
Soker, N. 2000, A&A, 357, 557
Stellingwerf, R. F. 1978, ApJ, 224, 953
Stobie, R. S. 1977, MNRAS, 180, 631
Szczerba, R., Siódmiak, N., Stasińska, G., & Borkowski, J. 2007, A&A, 469, 799
Tout, C. A., & Eggleton, P. P. 1988, MNRAS, 231, 823
Van Winckel, H. 1997, A&A, 319, 561
Van Winckel, H. 2003, ARA&A, 41, 391
Van Winckel, H. 2007, Baltic Astron., 16, 112
Van Winckel, H., Mathis, J. S., & Waelkens, C. 1992, Nature, 356, 500
Van Winckel, H., Waelkens, C., Waters, L. B. F. M., et al. 1998, A&A, 336, L17
Van Winckel, H., Waelkens, C., Fernie, J. D., & Waters, L. B. F. M. 1999, A&A, 343, 202
Waelkens, C., Van Winckel, H., Waters, L. B. F. M., & Bakker, E. J. 1996, A&A, 314, L17
Waters, L. B. F. M., Trams, N. R., & Waelkens, C. 1992, A&A, 262, L37
Zijlstra, A. A. 2007, Baltic Astron., 16, 79

Table 4. Individual heliocentric radial velocity datapoints of the programme stars.

JD(24+)	V(rad)	σ	JD(24+)	V(rad)	σ	JD(24+)	V(rad)	σ
IRAS 08544-4431								
51 146.7632	53.93	0.46	52 019.5475	65.09	0.82	52 736.5670	55.73	0.45
51 275.5548	58.82	0.67	52 020.5660	64.57	0.89	52 737.5675	55.23	0.66
51 276.5400	58.41	0.83	52 025.5503	62.85	0.89	52 738.5715	55.44	0.35
51 278.5411	58.55	0.69	52 026.5400	62.50	0.88	52 740.6439	54.65	0.34
51 282.5516	59.17	0.71	52 227.8345	54.60	0.36	52 983.7815	73.75	0.18
51 284.5721	59.32	0.65	52 229.8411	55.27	0.36	52 985.8487	75.66	0.91
51 467.8209	69.46	0.72	52 230.7878	55.48	0.47	52 986.7656	73.35	0.28
51 468.8564	68.67	0.63	52 231.8190	55.92	0.45	52 987.7777	72.92	0.20
51 510.8488	66.78	0.88	52 232.8366	56.32	0.47	52 988.7097	72.75	0.32
51 593.7902	60.27	0.51	52 233.8223	56.59	0.43	52 989.7627	72.25	0.35
51 596.5369	60.64	0.91	52 234.8312	56.93	0.43	52 990.7121	71.86	0.38
51 600.5514	58.22	0.43	52 235.8421	57.33	0.39	52 991.7597	71.52	0.47
51 603.5344	57.93	0.32	52 236.8460	57.39	0.44	52 992.7407	71.04	0.47
51 652.6373	53.56	0.25	52 237.8173	57.41	0.50	52 993.7198	70.53	0.50
51 655.6467	54.94	0.51	52 238.8600	57.51	0.47	52 994.8236	69.88	0.61
51 659.5312	56.51	0.26	52 239.8453	57.39	0.52	53 072.6987	56.49	0.67
51 716.4844	54.94	0.45	52 240.8067	57.35	0.56	53 073.6075	56.03	0.70
51 722.5308	56.82	0.45	52 272.7653	62.12	0.57	53 077.6309	55.84	0.99
51 726.4784	57.69	0.42	52 273.6877	62.32	0.42	53 078.6744	55.59	0.59
51 728.5054	58.24	0.41	52 274.7185	61.92	0.47	53 079.6282	56.25	0.85
51 730.4723	58.43	0.42	52 278.6249	61.41	0.37	53 083.6303	54.27	0.72
51 732.4845	58.61	0.48	52 279.7142	61.56	0.48	53 178.4623	53.52	0.44
51 816.8902	64.86	0.37	52 280.5488	61.87	0.45	53 179.4637	53.85	0.19
51 817.8948	64.60	0.39	52 281.7330	62.11	0.36	53 180.4955	54.40	0.80
51 818.9059	63.78	0.56	52 282.6908	62.63	0.25	53 182.4735	56.05	0.64
51 819.8806	64.79	0.40	52 282.6914	62.48	0.38	53 183.4791	55.77	0.37
51 820.8975	63.12	0.85	52 283.5876	62.60	0.33	53 184.4639	56.24	0.49
51 821.8891	62.68	0.55	52 284.6146	62.81	0.22	53 185.4616	57.85	0.78
51 822.8886	62.80	0.41	52 285.7966	63.59	0.33	53 187.4640	56.03	0.61
51 823.8627	62.33	0.43	52 285.8736	62.98	0.40	53 354.7158	65.77	0.66
51 824.8883	62.10	0.53	52 329.6329	62.15	0.71	53 356.6942	64.76	0.70
51 825.8752	61.63	0.51	52 330.6253	62.01	0.95	53 358.7105	63.70	0.78
51 826.8900	61.49	0.55	52 331.6184	61.97	0.83	53 360.7139	62.70	0.71
51 827.8881	61.55	0.59	52 332.6912	62.09	0.85	53 390.6954	63.46	0.81
51 828.8850	61.34	0.54	52 333.5833	61.89	0.94	53 394.7595	65.80	0.39
51 829.8889	61.03	0.30	52 334.6246	62.05	0.73	53 397.8360	67.23	0.35
51 881.8564	67.73	0.75	52 335.5591	62.19	0.87	53 402.8070	69.07	0.14
51 882.8542	68.19	0.74	52 336.6016	62.51	0.91	53 475.6505	71.21	0.50
51 886.7729	70.85	0.64	52 337.6051	62.72	0.91	53 481.6464	70.85	0.86
51 887.8017	71.15	0.59	52 338.5929	63.03	0.85	53 705.6999	55.87	0.28
51 890.7917	72.65	0.48	52 339.5910	63.10	0.71	53 706.6992	55.41	0.49
51 891.8222	72.72	0.51	52 340.6162	62.78	0.69	53 713.7763	53.82	0.67
51 892.8058	73.43	0.48	52 341.5897	63.06	0.79	53 833.6118	61.90	0.36
51 894.8195	73.29	0.67	52 571.8377	59.18	0.93	53 837.4779	62.28	0.58
51 940.7879	68.49	0.81	52 581.8738	58.91	0.46	54 077.8299	60.43	0.36
51 943.7737	69.84	0.63	52 727.5427	54.28	0.52	54 080.8300	60.65	0.18
51 944.5971	69.83	0.70	52 728.5978	54.28	0.39	54 180.5587	55.01	0.39
51 948.6634	71.90	0.66	52 729.5123	54.86	0.43	54 183.5442	55.84	0.38
51 951.7377	71.96	0.59	52 730.5892	54.87	0.43	54 190.5308	55.69	0.64
51 953.6671	71.86	0.63	52 731.5081	55.54	0.34	54 478.6732	68.75	0.33
52 015.5681	65.37	0.59	52 732.5623	55.61	0.43	54 479.6564	68.73	0.40
52 016.5395	65.55	0.63	52 733.5647	55.62	0.62	54 482.8249	69.43	0.40
52 017.5686	65.51	0.81	52 734.5704	55.79	0.50	54 486.7220	69.69	0.45
52 018.5751	65.03	0.84	52 735.5964	55.80	0.52			
IRAS 12222-4652								
45 397.800	7.44	.5	49 406.840	0.09	.5	52 340.7693	2.55	0.61
45 767.857	2.35	.5	49 407.826	−0.78	.5	52 469.6082	5.62	0.36
45 881.510	−1.29	.5	49 409.851	−1.43	.5	52 729.7034	11.28	0.24
47 913.900	5.4	1.0	49 522.582	0.90	.5	52 733.7608	10.55	0.35
47 914.900	2.8	1.0	49 526.659	0.81	.5	52 736.7651	8.16	0.47
47 915.800	4.4	1.0	50 527.749	3.7	1.0	52 739.6906	4.48	0.20
47 915.800	5.8	1.0	50 530.799	3.5	1.0	52 804.5557	2.05	0.11
47 917.800	6.6	1.0	51 594.8448	5.64	0.50	53 073.7687	1.21	0.37

Table 4. continued.

JD(24+)	V(rad)	σ	JD(24+)	V(rad)	σ	JD(24+)	V(rad)	σ
48 289.868	5.67	.5	51 766.5384	7.91	0.49	53 075.8142	1.01	0.37
48 312.794	0.07	.5	51 768.5061	6.09	0.44	53 076.8279	0.85	0.28
48 317.694	−0.12	.5	51 769.5234	5.43	0.38	53 078.8192	0.23	0.21
48 400.651	3.41	.5	51 771.4884	5.27	0.53	53 080.7999	0.33	0.26
48 453.476	1.74	.5	51 772.4816	5.40	0.60	53 085.7984	0.89	0.27
48 460.500	1.79	.5	51 945.7182	5.28	0.56	53 178.5860	−1.44	0.27
48 648.885	2.33	.5	52 016.7528	1.86	0.13	53 182.6712	−2.26	0.38
49 006.800	8.9	1.0	52 018.7552	2.25	0.18	53 185.6080	−2.15	0.23
49 031.800	5.8	1.0	52 021.7249	1.88	0.20	53 188.4618	−0.87	0.26
49 054.811	7.97	.5	52 024.6860	1.05	0.15	53 189.4601	−0.64	0.29
49 099.700	5.4	1.0	52 027.7294	1.69	0.15	53 399.8023	6.85	0.59
49 121.600	3.4	1.0	52 111.5528	2.93	0.40	53 402.8788	7.68	0.21
49 122.600	6.4	1.0	52 114.5745	1.98	0.40	53 475.7560	4.39	0.59
49 122.700	4.8	1.0	52 115.5823	1.58	0.20	53 478.7847	5.10	0.32
49 172.529	1.96	.5	52 118.5568	0.67	0.27	53 481.7560	5.61	0.89
49 189.500	7.	1.0	52 122.5608	−0.70	0.17	53 483.7766	5.04	0.24
49 190.600	7.6	1.0	52 329.8192	2.34	0.58	53 808.7140	8.26	0.71
49 191.500	8.5	1.0	52 332.8234	2.26	0.68	53 830.7574	2.47	1.04
49 334.800	−1.1	1.0	52 334.7261	2.18	0.60	53 833.7463	1.40	0.88
49 404.830	−1.42	.5	52 338.7713	2.64	0.53			
EN TrA								
48 312.891	−3.29	0.5	49 478.646	−29.4	1.0	52 339.9001	−25.78	0.16
48 324.812	−2.18	0.5	49 478.699	−29.8	1.0	52 417.6713	−22.85	0.47
48 327.796	−3.7	1.	49 485.839	−24.	1.0	52 425.6327	−26.47	0.23
48 329.854	−7.3	1.	49 774.878	−7.3	1.0	52 728.6876	−8.99	0.35
48 329.769	−6.5	1.	49 798.846	−9.26	0.5	52 731.7055	−8.60	0.55
48 329.855	−6.5	1.	49 831.822	−4.	1.0	52 803.6081	0.20	0.44
48 456.520	−0.07	0.5	49 953.507	−2.0	1.0	52 817.5814	−1.58	0.38
48 459.524	3.30	0.5	49 967.470	7.4	1.0	53 072.8237	−4.37	0.24
48 460.518	5.12	0.5	50 168.870	−0.9	1.0	53 073.7795	−3.75	0.27
48 461.513	5.24	0.5	50 189.870	10.2	1.0	53 078.8486	0.23	0.22
48 462.506	6.69	0.5	50 263.677	13.8	1.0	53 084.8179	5.47	0.33
48 732.817	5.9	1.0	50 276.5543	2.55	0.5	53 179.6833	2.12	0.35
48 842.506	2.1	1.0	50 496.865	−0.5	1.0	53 182.7142	2.23	0.04
48 844.516	−0.3	1.0	50 512.858	−1.5	1.0	53 185.6862	2.09	0.16
48 845.545	0.6	1.0	50 526.894	5.4	1.0	53 476.7417	−2.14	0.36
48 845.511	0.5	1.0	50 530.878	5.1	1.00	53 481.7673	0.23	0.38
48 846.515	0.6	1.0	50 532.901	3.2	1.00	53 830.7692	−21.91	0.45
49 031.842	−2.5	1.0	52 329.8257	−29.35	0.33	53 833.7578	−26.71	0.31
49 099.765	−0.6	1.0	52 332.8298	−29.26	0.06	53 837.6745	−31.87	0.70
49 121.681	−3.7	1.0	52 335.7537	−28.33	0.08	53 894.5700	−25.87	0.46
49 188.565	−11.9	1.0	52 337.8864	−27.22	0.14	53 896.7059	−24.65	0.84
IRAS 15469-5311								
51 277.7428	−23.28	0.50	52 115.6775	−9.76	0.70	53 074.8473	−17.24	0.27
51 278.6732	−23.20	0.55	52 116.7262	−9.94	0.49	53 075.8342	−16.32	0.21
51 469.4940	−5.99	0.23	52 117.5683	−9.07	0.47	53 076.8545	−16.92	0.24
51 471.5005	−6.71	0.38	52 118.6009	−8.90	0.24	53 077.8545	−17.00	0.20
51 478.5067	−10.32	0.58	52 122.5860	−10.05	0.19	53 078.8712	−16.61	0.65
51 593.8952	−27.10	0.49	52 123.6856	−10.10	0.15	53 079.8356	−17.57	0.38
51 595.8875	−26.71	0.19	52 278.8688	−12.72	0.48	53 081.8432	−17.80	0.20
51 597.8803	−26.39	0.35	52 279.8866	−11.88	0.31	53 083.8381	−19.06	0.35
51 599.8606	−25.19	0.42	52 280.8549	−13.11	0.52	53 084.8360	−16.68	0.36
51 601.8871	−24.05	0.47	52 281.8797	−13.64	0.18	53 085.8280	−17.15	0.11
51 603.8850	−23.69	0.83	52 283.8831	−15.29	0.25	53 182.7423	−26.95	0.45
51 652.7351	−22.93	0.23	52 284.8682	−16.01	0.38	53 183.6508	−26.38	0.33
51 652.7553	−22.46	0.09	52 285.8629	−15.71	0.38	53 184.6563	−27.14	0.78
51 654.7638	−22.67	0.31	52 329.8361	−20.85	0.36	53 185.6962	−26.24	0.48
51 659.7827	−21.98	0.42	52 330.8421	−21.35	0.14	53 187.6351	−23.49	0.79
51 716.5979	−14.11	0.31	52 331.8053	−21.56	0.35	53 228.5658	−19.17	0.25
51 718.6738	−14.00	0.27	52 333.8440	−21.91	0.12	53 230.6595	−18.30	0.20
51 729.7062	−12.17	0.43	52 334.7942	−22.23	0.11	53 231.5788	−18.26	0.21
51 730.7659	−11.77	0.34	52 336.8282	−21.36	0.52	53 232.5444	−17.87	0.05
51 732.7620	−11.74	0.33	52 337.7946	−22.11	0.27	53 391.8499	−3.47	0.76
51 760.5349	−4.76	0.45	52 338.8093	−24.81	0.56	53 397.7728	−4.73	0.68

Table 4. continued.

JD(24+)	V(rad)	σ	JD(24+)	V(rad)	σ	JD(24+)	V(rad)	σ
51 761.4994	−4.53	0.34	52 339.7781	−22.87	0.52	53 399.7905	−3.13	0.32
51 762.5343	−4.48	0.36	52 340.8450	−25.11	0.21	53 477.7892	−20.06	0.66
51 762.5467	−3.97	0.29	52 341.7736	−24.51	0.28	53 479.7884	−20.09	0.65
51 763.5447	−3.87	0.40	52 416.7697	−24.46	0.11	53 480.7505	−20.16	0.53
51 765.5127	−4.54	0.58	52 424.6481	−21.68	0.16	53 482.7946	−20.39	0.78
51 766.5339	−4.27	0.62	52 424.7176	−22.57	0.24	53 837.6853	−11.32	0.47
51 768.5679	−4.78	0.69	52 468.6674	−16.01	0.22	53 894.5796	−23.52	0.39
51 769.5646	−3.94	0.85	52 469.6336	−15.60	0.21	53 898.6560	−22.85	0.54
51 940.8625	−19.12	0.07	52 470.6850	−15.01	0.19	53 903.6450	−25.77	0.66
51 942.8880	−20.90	0.17	52 472.6732	−14.31	0.19	54 211.8782	−14.91	0.48
51 943.8385	−21.79	0.19	52 473.6416	−14.03	0.39	54 219.8503	−11.92	0.53
51 944.8526	−23.03	0.35	52 474.6498	−13.30	0.14	54 302.6379	−31.31	0.46
51 945.8252	−23.71	0.51	52 481.6175	−13.52	0.09	54 304.5784	−31.23	0.38
51 946.8458	−23.71	0.82	52 571.4983	−5.83	0.32	54 305.5780	−30.75	0.46
51 948.8802	−25.00	0.19	52 727.7383	−29.48	0.53	54 310.5047	−30.20	0.28
51 949.8475	−25.11	0.47	52 728.6970	−29.44	0.26	54 331.5914	−24.90	0.28
51 950.8386	−25.46	0.40	52 729.7127	−29.88	0.50	54 336.5006	−24.51	0.47
51 951.8346	−26.00	0.23	52 730.7218	−30.40	0.45	54 572.8004	−8.27	0.45
51 952.8300	−26.70	0.22	52 731.7150	−30.50	0.50	54 625.5740	−14.00	0.13
51 953.8449	−27.37	0.18	52 732.8830	−30.54	0.54	54 625.6043	−14.11	0.12
52 015.7748	−28.58	0.24	52 733.7957	−30.30	0.49	54 628.5107	−14.66	0.10
52 016.8033	−28.21	0.15	52 735.6860	−29.25	0.46	54 628.7443	−14.58	0.05
52 017.7562	−27.22	0.08	52 736.7746	−28.41	0.47	54 629.5725	−14.49	0.19
52 018.7724	−26.36	0.13	52 737.7340	−28.57	0.60	54 629.6498	−14.32	0.12
52 019.7750	−25.38	0.16	52 738.7553	−28.37	0.67	54 630.5171	−14.41	0.13
52 020.7769	−24.35	0.10	52 739.7448	−27.68	0.51	54 632.5266	−14.15	0.25
52 021.7452	−23.51	0.09	52 740.8043	−27.81	0.39	54 670.5925	−20.79	0.45
52 024.7130	−23.23	0.21	52 803.5603	−21.56	0.84	54 671.6170	−20.17	0.60
52 025.7119	−23.40	0.23	52 804.4995	−22.23	0.80	54 672.5327	−20.18	0.42
52 026.7477	−23.58	0.21	52 817.5699	−24.40	0.60	54 674.6597	−20.54	0.61
52 027.7771	−23.45	0.29	53 072.8326	−17.46	0.20	54 677.5327	−22.27	0.21
52 111.6771	−11.26	0.19	53 073.7938	−17.43	0.24	54 678.6760	−22.59	0.21
						54 679.6688	−22.68	0.16
IRAS 19125+0343								
51 277.9046	67.62	0.34	52 121.7094	75.54	0.71	53 180.7526	80.94	0.09
51 281.9142	67.48	0.61	52 123.7786	75.24	0.48	53 182.8327	81.45	0.11
51 469.5423	52.73	0.26	52 416.8105	55.29	0.13	53 183.7827	82.19	0.74
51 654.8809	79.72	0.66	52 417.8448	56.07	0.11	53 184.7404	79.96	0.16
51 655.8857	79.70	0.71	52 424.8240	55.49	0.48	53 184.7839	79.62	0.22
51 659.9231	81.77	0.36	52 468.8291	58.53	0.62	53 190.8718	75.60	0.22
51 760.6545	71.90	0.52	52 570.5382	66.61	0.31	53 191.8179	75.50	0.38
51 762.6816	70.35	0.32	52 571.5524	66.88	0.18	53 224.7553	75.40	0.20
51 763.6553	69.59	0.20	52 572.5529	66.49	0.54	53 232.7510	74.68	0.45
51 768.6680	68.74	0.13	52 573.5369	67.15	0.14	53 271.6065	75.07	0.30
51 773.7340	68.30	0.43	52 574.5574	68.15	0.08	53 273.5852	73.95	0.16
51 817.5984	64.36	0.26	52 575.5369	69.39	0.27	53 275.5725	72.53	0.09
51 819.5323	65.19	0.29	52 576.5504	70.35	0.20	53 278.5542	72.98	0.08
51 820.5569	65.97	0.36	52 577.5583	70.66	0.14	53 280.5621	73.21	0.27
51 821.5251	65.14	0.46	52 578.5386	70.56	0.32	53 283.5685	72.39	0.25
51 822.5530	64.91	0.05	52 579.5452	69.48	0.27	53 477.8754	54.14	0.35
51 823.5479	64.74	0.07	52 580.5299	67.78	0.51	53 479.8841	54.14	0.69
51 824.5235	64.72	0.14	52 581.5401	66.86	0.12	53 481.8821	54.62	0.65
51 825.5270	65.30	0.13	52 734.8964	77.60	0.12	53 482.8847	54.82	0.45
51 826.5340	66.08	0.11	52 735.8820	77.49	0.08	53 483.8867	54.77	0.36
51 827.5488	66.27	0.15	52 737.8768	76.76	0.08	53 648.5544	71.51	0.54
51 828.5417	66.19	0.14	52 738.9052	76.98	0.34	53 651.5256	73.75	0.31
52 015.9054	58.46	0.64	52 739.8834	77.10	0.28	53 653.5139	75.62	0.72
52 018.8886	60.38	0.14	52 740.8896	77.02	0.25	53 654.5258	75.79	0.94
52 024.8528	60.05	0.36	52 854.7053	64.85	0.07	53 898.8262	71.10	0.68
52 025.8665	59.34	0.15	52 857.6949	68.01	0.26	53 901.8042	69.85	0.66
52 026.8543	60.98	0.68	52 858.6964	69.00	0.28	53 954.7359	61.06	0.62
52 114.6868	76.02	0.18	52 866.6696	70.17	0.29	54 302.7889	72.11	0.59
52 115.6880	75.35	0.22	52 867.6726	68.24	0.36	54 303.7651	72.13	0.37
52 118.6850	75.39	0.31	53 179.7887	79.78	0.25	54 331.6422	73.60	0.82
						54 666.8072	73.13	0.53

Table 4. continued.

JD(24+)	V(rad)	σ	JD(24+)	V(rad)	σ	JD(24+)	V(rad)	σ
IRAS 19157-0247								
51 278.9071	23.53	0.27	52 416.8728	34.95	0.68	53 272.5760	39.39	1.02
51 280.9177	21.31	0.60	52 417.9179	37.25	0.92	53 273.5944	37.06	1.10
51 469.5487	37.83	0.63	52 571.5700	23.03	0.85	53 274.5934	38.01	0.19
51 471.5432	38.91	0.33	52 572.5797	26.16	0.94	53 275.5991	38.67	0.24
51 507.5279	25.58	0.90	52 574.5789	29.83	0.42	53 279.5319	42.27	0.20
51 652.9129	26.58	0.43	52 575.5604	30.82	0.72	53 281.5973	42.64	1.03
51 654.8925	27.64	0.40	52 576.5738	30.20	0.74	53 475.9058	29.89	0.50
51 760.6956	26.46	0.36	52 578.5621	27.82	0.27	53 476.9032	31.35	1.13
51 761.6696	28.09	0.31	52 579.5684	26.96	0.50	53 477.9035	34.83	0.00
51 762.7170	30.41	0.17	52 580.5533	25.16	1.05	53 478.9114	36.92	0.32
51 763.6769	32.51	0.26	52 581.5633	22.01	1.40	53 479.8996	38.47	0.12
51 765.6332	34.48	0.23	52 728.8557	20.67	0.58	53 481.9049	38.40	0.37
51 766.6211	35.12	0.27	52 734.8735	33.11	0.26	53 482.9121	39.90	0.86
51 769.7570	26.37	0.93	52 735.8335	33.70	0.33	53 483.9209	40.61	1.12
51 772.5723	24.10	0.17	52 736.8830	33.63	0.23	53 651.5721	27.45	0.73
51 816.5981	39.53	0.65	52 737.9002	32.41	0.20	53 652.5030	26.45	1.35
51 817.6263	39.84	0.28	52 738.8819	32.63	0.45	53 653.5579	26.00	0.80
51 819.5685	41.45	0.53	52 739.8598	32.19	0.50	53 809.8992	25.62	0.62
51 820.5746	43.44	0.46	52 740.9131	31.66	0.49	53 902.8038	27.46	0.19
51 821.5452	44.33	0.66	52 854.7293	33.04	0.50	53 903.8061	30.22	1.23
51 822.5745	43.81	0.39	52 855.7233	29.67	0.35	53 951.6950	35.49	1.18
51 823.5724	43.79	0.47	52 857.7190	27.54	0.52	53 954.7735	33.80	0.00
51 824.5479	41.91	0.81	52 859.7232	27.54	0.72	53 956.7439	33.99	1.09
51 825.5514	38.89	1.16	52 861.7367	27.65	0.09	53 960.7338	41.74	1.15
51 826.5596	36.03	1.04	52 862.7190	26.11	0.25	54 303.7769	33.05	0.83
51 827.5749	36.71	0.38	52 865.7062	26.99	0.33	54 305.8161	37.83	0.54
51 828.5661	37.19	0.39	52 867.6963	33.14	0.23	54 308.7831	44.33	0.64
51 829.5199	38.42	0.18	53 179.8589	25.49	0.20	54 581.9151	44.84	1.11
51 829.5403	38.17	0.27	53 179.8946	26.30	1.00	54 625.8859	28.83	1.48
52 020.8803	36.02	0.43	53 184.8284	25.87	1.37	54 626.8699	28.58	0.61
52 025.8955	27.45	0.36	53 188.8789	25.64	0.60	54 628.7670	27.76	0.71
52 026.8832	28.65	0.32	53 190.8982	24.37	1.44	54 630.7473	27.48	0.32
52 027.8899	29.46	0.19	53 191.8399	24.05	0.75	54 630.7917	28.22	1.33
52 114.8391	29.58	1.12	53 224.7904	33.36	0.54	54 632.7171	28.95	1.20
52 116.8258	28.42	1.29	53 232.7181	34.83	0.28	54 666.8228	33.33	0.37
52 227.5114	29.59	0.32	53 270.5775	38.37	0.72	54 672.7039	32.89	0.90
52 227.5322	29.76	0.21	53 271.6303	39.54	0.82	54 675.7832	37.97	1.40

Table 5. Individual photometric datapoints of the programme stars obtained at SAAO.

HJD	V	$B-V$	$U-B$	$V-R$	$V-I$	HJD	V	$B-V$	$U-B$	$V-R$	$V-I$
IRAS 08544-4431											
2 450 858.47530	9.149	1.553	1.180	0.995	2.029	2 451 581.33470	9.163	1.580	1.191	0.992	2.042
2 450 866.39190	9.164	1.555	1.167	0.993	2.025	2 451 582.39140	9.169	1.583	1.188	0.997	2.046
2 450 867.38350	9.156	1.547	1.169	0.990	2.018	2 451 608.44360	9.035	1.511	1.148	0.961	1.982
2 450 868.39470	9.168	1.546	1.154	0.990	2.017	2 451 609.37170	9.017	1.516	1.127	0.965	1.993
2 450 869.41250	9.153	1.545	1.157	0.994	2.026	2 451 625.28560	9.071	1.547	1.176	0.977	2.014
2 450 871.39890	9.151	1.540	1.151	0.994	2.020	2 451 626.29140	9.072	1.547	1.173	0.977	2.017
2 450 872.40870	9.169	1.541	1.158	0.999	2.011	2 451 663.23130	9.133	1.548	1.162	0.979	2.036
2 450 874.38380	9.158	1.536	1.156	0.992	2.014	2 451 666.22130	9.106	1.538	1.155	0.972	2.014
2 450 879.39550	9.163	1.532	1.160	0.984	2.005	2 451 929.49208	9.142	1.548	1.162	0.995	2.021
2 450 883.34250	9.140	1.539	1.161	0.983	2.010	2 451 930.48697	9.149	1.547	1.180	0.996	2.026
2 450 884.46330	9.167	1.537	1.149	0.997	2.014	2 451 931.49118	9.163	1.547	1.189	1.001	2.036
2 450 885.37300	9.133	1.538	1.193	0.990	2.006	2 451 936.49577	9.180	1.555	1.190	1.000	2.028
2 450 886.41580	9.127	1.536	1.190	0.984	2.013	2 451 939.53417	9.174	1.566	1.326	1.005	2.043
2 450 887.44010	9.123	1.544	1.163	0.992	2.017	2 451 941.48938	9.168	1.561	1.196	1.006	2.037
2 450 889.44560	9.122	1.544	1.165	0.996	2.021	2 451 944.48373	9.167	1.550	1.158	1.005	2.039
2 450 918.28290	9.144	1.555	1.178	0.989	2.023	2 451 945.50376	9.175	1.555	1.150	1.002	2.038
2 450 919.28720	9.148	1.552	1.175	0.994	2.027	2 451 956.47669	9.129	1.557	1.188	1.001	2.038
2 450 929.29080	9.180	1.541	1.144	0.996	2.022	2 451 957.45032	9.125	1.549	1.170	1.002	2.032
2 450 931.32500	9.173	1.542	1.149	0.994	2.023	2 451 960.40009	9.122	1.541	1.153	1.001	2.031
2 450 937.26810	9.160	1.544	1.143	0.997	2.033	2 451 961.44573	9.112	1.543	1.157	0.993	2.022
2 450 948.26710	9.116	1.540	1.152	0.989	2.017	2 451 962.44569	9.112	1.540	1.154	0.990	2.020
2 450 957.21450	9.110	1.522	1.136	0.984	2.010	2 451 963.44349	9.106	1.531	1.120	0.984	2.019
2 450 959.21680	9.114	1.523	1.145	0.982	2.011	2 451 964.44258	9.113	1.544	1.149	0.988	2.023
2 451 205.47480	9.143	1.540	1.165	0.990	2.030	2 451 965.44219	9.110	1.538	1.160	0.996	2.018
2 451 209.41850	9.132	1.554	1.161	0.999	2.034	2 451 969.45933	9.098	1.537	1.163	0.984	2.016
2 451 210.39440	9.139	1.553	1.196	0.995	2.031	2 451 970.47381	9.098	1.526	1.148	0.986	2.006
2 451 215.42880	9.155	1.549	1.196	0.996	2.033	2 451 972.38308	9.082	1.533	1.183	0.991	2.018
2 451 216.40510	9.148	1.555	1.179	0.994	2.026	2 451 976.44461	9.082	1.549	1.462	0.985	2.014
2 451 228.38630	9.148	1.559	1.190	0.991	2.028	2 451 981.36532	9.087	1.538	1.289	0.988	2.016
2 451 230.37560	9.138	1.553	1.175	0.988	2.024	2 451 982.36317	9.080	1.530	1.200	0.994	2.021
2 451 231.37210	9.142	1.546	1.178	0.992	2.027	2 451 988.35682	9.101	1.529	1.144	0.990	2.024
2 451 232.36380	9.145	1.549	1.193	0.990	2.026	2 452 002.34988	9.093	1.537	1.142	0.994	2.022
2 451 233.36640	9.145	1.549	1.181	0.991	2.023	2 452 003.37655	9.093	1.529	1.139	0.991	2.028
2 451 234.34890	9.146	1.543	1.177	0.993	2.030	2 452 011.34254	9.081	1.537	1.173	0.988	2.020
2 451 235.35870	9.143	1.541	1.188	0.997	2.028	2 452 012.35521	9.086	1.536	1.183	0.986	2.024
2 451 236.34840	9.136	1.545	1.175	0.987	2.016	2 452 019.25966	9.113	1.533	1.150	0.992	2.027
2 451 238.33990	9.128	1.537	1.161	0.993	2.021	2 452 022.27246	9.122	1.532	1.145	0.993	2.027
2 451 239.34330	9.124	1.548	1.200	0.985	2.016	2 452 030.23594	9.128	1.528	1.139	0.990	2.021
2 451 240.37060	9.132	1.535	1.211	0.992	2.020	2 452 033.27647	9.131	1.537	1.183	0.980	2.023
2 451 298.24170	9.192	1.575	1.178	1.007	2.056	2 452 041.25064	9.142	1.544	1.159	0.994	2.027
2 451 300.23330	9.192	1.564	1.226	1.006	2.053	2 452 042.24695	9.141	1.543	1.141	0.998	2.032
2 451 303.24530	9.170	1.557	1.182	0.997	2.040	2 452 043.23925	9.137	1.541	1.144	0.984	2.015
2 451 309.23600	9.154	1.548	1.169	0.999	2.040	2 452 045.25507	9.130	1.545	1.142	0.989	2.033
2 451 576.40290	9.179	1.589	1.203	0.996	2.050	2 452 057.26545	9.080	1.529	1.117	0.986	2.020
2 451 579.40000	9.168	1.580	1.213	0.993	2.049	2 452 060.29439	9.062	1.533	1.140	0.990	2.027
2 451 580.35280	9.167	1.582	1.183	0.993	2.046						
IRAS 12222-4652											
2 451 625.4862	7.977	0.426	0.345	0.265	0.528	2 452 428.3283	7.936	0.423	0.335	0.255	0.523
2 451 626.5038	8.005	0.425	0.334	0.274	0.542	2 452 429.2922	7.929	0.421	0.329	0.255	0.519
2 451 663.3917	7.972	0.423	0.337	0.259	0.519	2 452 430.2371	7.935	0.422	0.345	0.239	0.510
2 451 688.3192	7.937	0.408	0.342	0.248	0.507	2 452 431.2499	7.937	0.414	0.337	0.247	0.520
2 451 691.4224	7.957	0.421	0.330	0.257	0.516	2 452 440.2451	7.889	0.397	0.337	0.213	0.485
2 451 692.3194	7.965	0.417	0.342	0.256	0.525	2 452 441.2684	7.869	0.404	0.313	0.239	0.497
2 451 712.2471	7.917	0.408	0.337	0.250	0.509	2 452 445.2723	7.889	0.404	0.332	0.243	0.491
2 451 976.5085	8.004	0.433	0.369	0.267	0.544	2 452 450.2713	7.917	0.405	0.334	0.248	0.508
2 451 977.5076	8.011	0.441	0.364	0.272	0.540	2 452 458.2337	7.966	0.417	0.349	0.250	0.531
2 451 978.4812	8.005	0.425	0.358	0.271	0.546	2 452 684.5593	7.880	0.402	0.331	0.245	0.492
2 451 980.5089	8.004	0.434	0.324	0.271	0.541	2 452 686.5516	7.876	0.402	0.331	0.239	0.495
2 451 981.5092	8.002	0.433	0.364	0.269	0.536	2 452 687.5810	7.881	0.403	0.328	0.244	0.498
2 451 982.4785	8.006	0.433	0.359	0.268	0.547	2 452 690.5702	7.892	0.402	0.331	0.242	0.493
2 451 988.5325	7.983	0.432	0.340	0.261	0.523	2 452 691.5556	7.917	0.408	0.344	0.243	0.492
2 452 017.3946	7.922	0.398	0.335	0.248	0.504	2 452 692.5686	7.936	0.411	0.344	0.251	0.506
2 452 017.4016	7.919	0.399	0.329	0.250	0.508	2 452 693.5684	7.944	0.413	0.343	0.250	0.508
2 452 018.5058	7.921	0.402	0.338	0.243	0.502	2 452 701.5593	7.994	0.431	0.352	0.255	0.522

Table 5. continued.

HJD	V	$B-V$	$U-B$	$V-R$	$V-I$	HJD	V	$B-V$	$U-B$	$V-R$	$V-I$
2 452 019.3085	7.915	0.403	0.345	0.246	0.501	2 452 705.5750	8.009	0.444	0.348	0.266	0.540
2 452 022.3214	7.941	0.414	0.339	0.250	0.509	2 452 706.5443	8.022	0.453	0.347	0.270	0.541
2 452 025.4453	7.961	0.415	0.338	0.257	0.519	2 452 707.5710	8.024	0.456	0.346	0.276	0.545
2 452 029.3838	7.985	0.433	0.350	0.264	0.533	2 452 710.5422	8.017	0.456	0.354	0.277	0.559
2 452 030.2856	7.979	0.435	0.343	0.258	0.531	2 452 725.5131	7.891	0.407	0.320	0.242	0.505
2 452 033.3263	7.970	0.431	0.341	0.262	0.533	2 452 726.4868	7.876	0.404	0.313	0.241	0.500
2 452 033.3603	7.983	0.431	0.340	0.260	0.533	2 452 727.5105	7.866	0.392	0.318	0.239	0.495
2 452 037.3227	7.972	0.418	0.335	0.257	0.531	2 452 728.5041	7.861	0.395	0.311	0.239	0.494
2 452 038.3380	7.969	0.415	0.329	0.259	0.529	2 452 729.4815	7.852	0.386	0.312	0.237	0.495
2 452 040.3509	7.958	0.418	0.332	0.260	0.529	2 452 730.4904	7.837	0.395	0.301	0.236	0.493
2 452 041.3004	7.964	0.421	0.326	0.261	0.529	2 452 731.5323	7.858	0.389	0.299	0.240	0.499
2 452 041.3152	7.964	0.420	0.331	0.259	0.524	2 452 732.4831	7.839	0.393	0.294	0.238	0.495
2 452 042.2969	7.961	0.414	0.332	0.262	0.530	2 452 733.4773	7.840	0.395	0.301	0.231	0.489
2 452 042.3178	7.957	0.426	0.329	0.261	0.523	2 452 734.4769	7.834	0.391	0.299	0.236	0.491
2 452 043.2893	7.952	0.423	0.324	0.256	0.523	2 452 753.4278	7.965	0.421	0.333	0.252	0.521
2 452 045.2852	7.950	0.424	0.335	0.260	0.533	2 452 754.4274	7.967	0.421	0.338	0.251	0.518
2 452 057.2957	7.917	0.404	0.319	0.244	0.506	2 452 755.4106	7.972	0.422	0.339	0.254	0.524
2 452 057.3704	7.923	0.406	0.308	0.253	0.517	2 452 756.4091	7.968	0.424	0.340	0.253	0.520
2 452 060.3245	7.922	0.410	0.330	0.251	0.512	2 452 759.4382	8.000	0.429	0.344	0.257	0.531
2 452 061.2747	7.902	0.415	0.337	0.248	0.509	2 452 762.4125	8.005	0.440	0.336	0.260	0.533
2 452 072.3048	8.003	0.436	0.328	0.276	0.545	2 452 766.4175	8.013	0.436	0.350	0.265	0.537
2 452 073.2156	7.974	0.418	0.343	0.258	0.526	2 452 778.3267	7.999	0.431	0.338	0.268	0.536
2 452 073.2555	7.965	0.419	0.351	0.259	0.526	2 452 779.3598	8.032	0.452	0.359	0.035	0.488
2 452 074.2161	7.954	0.423	0.334	0.255	0.526	2 452 781.4304	7.966	0.414	0.308	0.253	0.521
2 452 075.2183	7.965	0.416	0.342	0.252	0.531	2 452 783.3404	7.957	0.414	0.328	0.257	0.519
2 452 075.2587	7.965	0.404	0.338	0.274	0.540	2 452 789.3391	7.882	0.394	0.323	0.241	0.493
2 452 076.2181	7.958	0.419	0.343	0.251	0.528	2 453 039.6049	7.937	0.413	0.317	0.248	0.507
2 452 076.2558	7.957	0.411	0.339	0.264	0.533	2 453 040.5528	7.961	0.419	0.316	0.252	0.511
2 452 080.2331	7.978	0.433	0.351	0.267	0.535	2 453 041.5818	7.929	0.401	0.329	0.253	0.507
2 452 080.2653	7.981	0.425	0.345	0.273	0.543	2 453 044.5784	7.915	0.401	0.313	0.245	0.502
2 452 081.2366	7.996	0.427	0.346	0.260	0.536	2 453 045.5349	7.921	0.399	0.287	0.238	0.489
2 452 081.2559	7.979	0.428	0.343	0.264	0.536	2 453 055.5898	7.895	0.402	0.323	0.241	0.500
2 452 082.2652	7.975	0.443	0.347	0.256	0.542	2 453 057.5522	7.906	0.404	0.338	0.246	0.499
2 452 087.2278	7.986	0.435	0.355	0.262	0.544	2 453 063.5137	7.922	0.417	0.338	0.239	0.503
2 452 087.2564	7.979	0.434	0.344	0.267	0.538	2 453 065.5130	7.927	0.420	0.335	0.249	0.511
2 452 093.2241	7.971	0.429	0.342	0.265	0.541	2 453 067.5134	7.929	0.422	0.333	0.246	0.511
2 452 112.2266	7.946	0.401	0.335	0.251	0.519	2 453 068.5419	7.937	0.414	0.346	0.255	0.512
2 452 319.5708	7.939	0.403	0.331	0.248	0.503	2 453 079.4706	7.989	0.440	0.341	0.258	0.534
2 452 320.5606	7.950	0.413	0.337	0.242	0.497	2 453 087.4741	7.995	0.431	0.339	0.262	0.528
2 452 321.5606	7.949	0.413	0.338	0.241	0.497	2 453 109.4551	7.860	0.393	0.329	0.230	0.482
2 452 322.5773	7.955	0.414	0.333	0.255	0.512	2 453 113.3709	7.886	0.392	0.330	0.237	0.489
2 452 324.5259	7.962	0.410	0.346	0.260	0.520	2 453 118.3713	7.904	0.394	0.319	0.246	0.492
2 452 324.6051	7.956	0.414	0.340	0.247	0.509	2 453 119.3629	7.906	0.400	0.328	0.242	0.494
2 452 327.5389	7.956	0.420	0.335	0.261	0.518	2 453 121.4304	7.905	0.395	0.331	0.251	0.504
2 452 336.5080	7.931	0.415	0.347	0.244	0.506	2 453 123.3593	7.948	0.408	0.333	0.241	0.501
2 452 346.5020	7.965	0.420	0.343	0.267	0.523	2 453 124.3617	7.958	0.407	0.329	0.248	0.505
2 452 347.5431	7.954	0.425	0.340	0.259	0.520	2 453 129.3564	8.005	0.427	0.342	0.264	0.530
2 452 348.5020	7.955	0.425	0.355	0.255	0.518	2 453 137.3513	8.022	0.455	0.359	0.281	0.552
2 452 349.5037	7.964	0.426	0.353	0.258	0.516	2 453 139.3497	8.048	0.458	0.367	0.277	0.550
2 452 350.5134	7.961	0.426	0.346	0.258	0.518	2 453 140.3455	8.037	0.462	0.351	0.271	0.549
2 452 352.4633	7.964	0.427	0.353	0.256	0.521	2 453 142.3413	8.036	0.465	0.350	0.275	0.547
2 452 356.4939	7.945	0.419	0.348	0.264	0.518	2 453 144.2756	8.021	0.461	0.347	0.276	0.556
2 452 357.5297	7.946	0.419	0.349	0.250	0.513	2 453 146.3328	8.008	0.453	0.343	0.270	0.551
2 452 376.3944	7.989	0.418	0.347	0.285	0.550	2 453 147.3217	8.005	0.455	0.335	0.269	0.544
2 452 377.3793	7.954	0.431	0.356	0.264	0.529	2 453 152.2814	7.979	0.443	0.331	0.256	0.532
2 452 381.4302	7.952	0.418	0.339	0.254	0.519	2 453 156.2780	7.924	0.416	0.306	0.248	0.511
2 452 383.3994	7.947	0.417	0.340	0.261	0.523	2 453 158.3357	7.922	0.405	0.305	0.243	0.504
2 452 384.3629	7.940	0.407	0.347	0.250	0.517	2 453 173.2689	7.865	0.385	0.315	0.231	0.480
2 452 403.4261	7.979	0.420	0.349	0.254	0.520	2 453 174.2657	7.870	0.386	0.318	0.232	0.480
2 452 404.3022	8.002	0.426	0.347	0.259	0.534	2 453 178.2723	7.902	0.403	0.319	0.247	0.506
2 452 405.3038	7.985	0.432	0.356	0.257	0.519	2 453 180.2890	7.920	0.410	0.325	0.249	0.505
2 452 408.3870	7.993	0.434	0.338	0.264	0.542	2 453 181.2758	7.924	0.416	0.328	0.249	0.506
2 452 410.3089	7.995	0.445	0.362	0.262	0.538	2 453 184.2745	7.953	0.426	0.316	0.250	0.516

Table 5. continued.

HJD	V	$B-V$	$U-B$	$V-R$	$V-I$	HJD	V	$B-V$	$U-B$	$V-R$	$V-I$
2 452 412.2881	7.999	0.446	0.355	0.265	0.540	2 453 185.2637	7.980	0.412	0.334	0.265	0.530
2 452 413.3215	8.013	0.450	0.366	0.243	0.516	2 453 193.2971	8.008	0.431	0.338	0.259	0.530
2 452 414.2939	7.987	0.435	0.346	0.261	0.538	2 453 194.2470	8.009	0.445	0.326	0.260	0.530
2 452 426.2840	7.961	0.425	0.343	0.266	0.536	2 453 195.2581	8.017	0.441	0.322	0.264	0.536
IRAS 15469-5311											
2 448 803.3438	10.518	1.428	1.064	0.890	1.823	2 449 213.2441	10.572	1.434	1.058	0.897	1.824
2 448 829.3045	10.589	1.446	1.048	0.895	1.832	2 449 434.5918	10.567	1.447	1.072	0.902	1.840
2 448 834.3133	10.580	1.442	1.065	0.888	1.835	2 449 438.6216	10.596	1.436	0.938	0.892	1.816
2 448 844.2302	10.573	1.444	1.09	0.898	1.838	2 449 442.6260	10.622	1.468	0.973	0.904	1.853
2 449 091.5265	10.540	1.432	1.037	0.888	1.815	2 449 485.4741	10.532	1.438	1.050	0.891	1.820
2 449 093.5068	10.569	1.441	1.046	0.898	1.830	2 449 489.4590	10.493	1.428	1.064	0.884	1.817
2 449 098.5501	10.578	1.450	1.043	0.895	1.826	2 449 490.4805	10.520	1.448	1.076	0.897	1.829
2 449 102.6072	10.616	1.457	1.070	0.905	1.832	2 449 495.4346	10.503	1.426	1.036	0.895	1.821
2 449 104.5423	10.593	1.449	1.040	0.899	1.828	2 449 498.5151	10.507	1.445	1.066	0.890	1.824
2 449 107.5335	10.607	1.456	1.050	0.901	1.836	2 449 503.4702	10.525	1.432	1.080	0.892	1.824
2 449 112.4527	10.581	1.459	1.009	0.896	1.829	2 449 510.4556	10.550	1.428	1.042	0.887	1.807
2 449 115.4539	10.585	1.437	1.074	0.914	1.831	2 449 513.4326	10.565	1.433	1.050	0.892	1.822
2 449 120.4480	10.555	1.437	1.045	0.897	1.827	2 449 515.3564	10.562	1.437	1.062	0.893	1.825
2 449 124.5799	10.529	1.436	1.031	0.890	1.817	2 449 518.4131	10.556	1.441	1.058	0.896	1.820
2 449 126.4214	10.527	1.438	1.036	0.890	1.817	2 449 534.4077	10.573	1.440	1.101	0.895	1.819
2 449 128.4615	10.537	1.425	1.045	0.894	1.819	2 449 537.3081	10.553	1.434	1.056	0.890	1.810
2 449 125.5241	10.538	1.431	1.025	0.891	1.819	2 449 539.3550	10.545	1.430	1.056	0.890	1.814
2 449 138.3878	10.582	1.446	1.04	0.895	1.818	2 449 544.3740	10.532	1.433	1.060	0.892	1.808
2 449 142.3606	10.573	1.456	1.061	0.886	1.821	2 449 562.2744	10.530	1.424	1.053	0.885	1.814
2 449 146.4118	10.571	1.449	1.079	0.899	1.833	2 449 566.2617	10.543	1.438	1.062	0.887	1.816
2 449 147.3900	10.563	1.445	1.085	0.895	1.830	2 449 574.2617	10.605	1.435	1.034	0.885	1.792
2 449 156.4061	10.525	1.420	1.030	0.887	1.804	2 449 582.2446	10.571	1.457	1.085	0.900	1.842
2 449 168.3833	10.543	1.442	1.075	0.881	1.801	2 451 626.5864	10.516	1.434	0.981	0.889	1.826
2 449 172.3808	10.567	1.436	1.056	0.891	1.810	2 451 712.3599	10.527	1.479	1.131	0.894	1.808
2 449 209.3057	10.522	1.430	1.028	0.888	1.807						
IRAS 19125+0343											
2 449 485.5996	10.136	1.003	0.644	0.675	1.458	2 449 561.3525	10.112	0.993	0.624	0.672	1.450
2 449 489.5518	10.137	1.013	0.655	0.674	1.466	2 449 563.4150	10.100	0.997	0.627	0.662	1.439
2 449 492.5127	10.110	1.010	0.649	0.666	1.459	2 449 575.4209	10.155	1.011	0.673	0.674	1.462
2 449 495.5205	10.136	1.008	0.617	0.672	1.467	2 449 587.3325	10.186	1.032	0.696	0.683	1.483
2 449 497.5693	10.139	0.995	0.627	0.673	1.472	2 449 590.3867	10.143	1.011	0.684	0.683	1.472
2 449 502.5557	10.201	1.005	0.663	0.667	1.438	2 449 595.2964	10.116	0.996	0.685	0.660	1.454
2 449 510.5547	10.215	1.022	0.684	0.683	1.484	2 449 598.3110	10.122	0.982	0.612	0.663	1.441
2 449 513.4912	10.196	1.016	0.667	0.690	1.491	2 449 603.2734	10.147	1.023	0.624	0.675	1.466
2 449 515.4893	10.196	1.016	0.668	0.687	1.485	2 449 607.2588	10.165	1.003	0.657	0.679	1.482
2 449 518.5161	10.200	1.028	0.672	0.686	1.493	2 449 621.2637	10.187	1.029	0.660	0.688	1.499
2 449 534.4951	10.148	1.004	0.655	0.671	1.461	2 449 624.2871	10.185	1.018	0.679	0.684	1.489
2 449 538.5215	10.177	1.014	0.648	0.674	1.465	2 449 629.2793	10.149	1.021	0.655	0.687	1.490
2 449 539.4331	10.174	1.015	0.651	0.677	1.472	2 451 626.6389	10.125	1.007	0.595	0.675	1.457
2 449 544.4565	10.196	1.018	0.672	0.680	1.468	2 451 816.2607	10.197	1.018	0.660	0.684	1.492
2 449 547.4580	10.197	1.014	0.665	0.688	1.482	2 451 819.3136	10.191	1.023	0.646	0.685	1.482
IRAS 19157-0247											
2 448 404.634	10.740	0.856	0.590	0.530	1.115	2 449 147.5633	10.674	0.802	0.535	0.516	1.061
2 448 406.616	10.740	0.854	0.594	0.535	1.111	2 449 170.4974	10.740	0.800	0.524	0.499	1.042
2 448 408.640	10.719	0.843	0.580	0.515	1.087	2 449 183.5664	10.689	0.801	0.487	0.509	1.062
2 448 409.557	10.703	0.823	0.547	0.519	1.080	2 449 188.5495	10.694	0.815	0.522	0.518	1.077
2 448 412.583	10.672	0.800	0.514	0.501	1.045	2 449 207.4435	10.624	0.774	0.464	0.498	1.036
2 448 417.533	10.668	0.806	0.540	0.512	1.073	2 449 213.3872	10.733	0.817	0.529	0.512	1.066
2 448 419.530	10.672	0.814	0.551	0.512	1.070	2 449 228.2715	10.699	0.840	0.542	0.517	1.098
2 448 427.484	10.720	0.817	0.586	0.509	1.073	2 449 232.3948	10.736	0.855	0.588	0.538	1.110
2 448 434.514	10.696	0.818	0.535	0.507	1.082	2 449 244.3211	10.700	0.806	0.527	0.510	1.062
2 448 435.486	10.703	0.818	0.512	0.517	1.087	2 449 245.3233	10.680	0.806	0.534	0.510	1.059
2 448 436.507	10.727	0.823	0.527	0.516	1.083	2 451 626.6478	10.662	0.876	0.571	0.508	1.065
2 448 437.490	10.720	0.810	0.535	0.518	1.082	2 451 692.6036	10.659	0.798	0.544	0.522	1.067
2 448 454.465	10.688	0.825	0.559	0.521	1.088	2 451 746.4517	10.713	0.804	0.516	0.508	1.056
2 448 456.432	10.674	0.806	0.516	0.514	1.081	2 451 747.4226	10.710	0.800	0.500	0.502	1.052
2 448 457.433	10.669	0.816	0.516	0.514	1.067	2 451 751.4427	10.697	0.811	0.504	0.511	1.062
2 448 462.416	10.650	0.799	0.496	0.509	1.065	2 451 752.5005	10.724	0.828	0.532	0.523	1.077
2 448 480.470	10.726	0.801	0.511	0.509	1.083	2 451 761.4192	10.753	0.852	0.555	0.540	1.121
2 448 483.370	10.698	0.807	0.511	0.503	1.062	2 451 762.3703	10.736	0.844	0.555	0.525	1.097

Table 5. continued.

HJD	V	$B-V$	$U-B$	$V-R$	$V-I$	HJD	V	$B-V$	$U-B$	$V-R$	$V-I$
2 448 500.383	10.696	0.819	0.538	0.518	1.089	2 451 772.3775	10.729	0.840	0.529	0.511	1.077
2 448 511.324	10.719	0.813	0.518	0.522	1.087	2 451 773.3774	10.736	0.835	0.524	0.511	1.077
2 448 799.5644	10.692	0.810	0.540	0.516	1.088	2 451 782.3920	10.664	0.820	0.534	0.511	1.072
2 448 828.4964	10.630	0.806	0.534	0.507	1.072	2 451 784.3776	10.650	0.803	0.503	0.508	1.057
2 448 843.3588	10.672	0.808	0.541	0.516	1.084	2 451 786.3757	10.682	0.801	0.498	0.505	1.049
2 449 138.5385	10.708	0.815	0.563	0.524	1.085	2 451 816.2680	10.739	0.824	0.565	0.525	1.091
2 449 146.5408	10.644	0.793	0.510	0.511	1.067	2 451 819.3207	10.725	0.846	0.547	0.524	1.092

Table 6. Individual photometric datapoints of the programme stars obtained with the Geneva P7 photometer, both on the Swiss telescope at La Silla and on the Flemish 1.2 m Mercator telescope.

HJD(24+)	V	$[U-B]$	$[V-B]$	$[B1-B]$	$[B2-B]$	$[V1-B]$	$[G-B]$	Weight(mag)	Weight(colour)
IRAS 12222-4652									
47 258.707	7.930	1.961	0.451	0.993	1.377	1.177	1.509	2	2
47 261.651	7.943	1.952	0.454	0.996	1.380	1.186	1.516	3	3
47 264.569	7.934	1.959	0.460	0.989	1.386	1.192	1.547	2	3
47 266.642	7.882	1.959	0.473	0.986	1.385	1.206	1.547	1	0
47 269.556	7.931	1.946	0.453	0.988	1.389	1.183	1.525	3	3
47 273.552	7.920	1.954	0.462	0.989	1.392	1.195	1.535	3	3
47 276.551	7.922	1.946	0.457	0.995	1.389	1.190	1.529	3	3
47 282.624	7.930	1.941	0.446	0.988	1.390	1.183	1.522	3	3
47 284.625	7.924	1.960	0.457	0.998	1.388	1.183	1.528	3	3
47 289.644	7.919	1.946	0.474	0.984	1.392	1.207	1.546	2	3
47 296.656	7.958	1.951	0.477	0.990	1.386	1.211	1.549	0	2
47 304.565	7.905	1.958	0.472	0.992	1.393	1.207	1.547	3	3
47 308.600	7.916	1.977	0.462	0.995	1.389	1.200	1.533	3	3
47 315.589	7.944	1.952	0.454	0.993	1.395	1.183	1.525	3	3
47 493.816	7.894	1.939	0.477	0.989	1.396	1.211	1.552	3	3
47 495.814	7.896	1.934	0.472	0.979	1.393	1.197	1.548	3	3
47 505.839	7.906	1.946	0.468	0.985	1.383	1.204	1.549	3	4
47 519.850	7.932	1.963	0.440	0.990	1.383	1.173	1.512	3	3
47 521.832	7.945	1.954	0.432	0.995	1.368	1.174	1.501	3	3
47 537.845	7.935	1.973	0.456	0.996	1.388	1.187	1.532	4	4
47 540.844	7.945	1.962	0.447	0.999	1.380	1.177	1.521	4	4
47 542.844	7.938	1.983	0.447	0.997	1.382	1.183	1.524	3	3
47 544.821	7.934	1.981	0.441	1.000	1.375	1.180	1.512	3	3
47 546.849	7.928	1.982	0.457	1.003	1.387	1.183	1.529	3	3
47 549.823	7.945	1.967	0.447	0.998	1.387	1.184	1.521	3	3
47 551.838	7.915	1.974	0.463	0.995	1.384	1.197	1.532	3	3
47 596.748	7.944	1.964	0.439	1.001	1.376	1.170	1.502	3	3
47 598.772	7.941	1.966	0.439	1.003	1.369	1.175	1.511	3	3
47 600.764	7.937	1.947	0.450	0.998	1.382	1.183	1.516	3	3
47 601.733	7.928	1.956	0.463	0.996	1.390	1.197	1.526	2	3
47 602.692	7.916	1.959	0.457	0.990	1.388	1.183	1.534	3	3
47 605.675	7.928	1.976	0.458	0.991	1.393	1.189	1.526	3	4
47 606.673	7.936	1.961	0.455	0.987	1.382	1.185	1.527	3	3
47 607.669	7.932	1.953	0.457	0.985	1.383	1.187	1.530	2	2
47 608.714	7.925	1.952	0.460	0.986	1.385	1.189	1.522	3	3
47 609.733	7.913	1.962	0.461	0.995	1.387	1.192	1.540	2	3
47 610.678	7.914	1.946	0.468	0.985	1.388	1.198	1.537	2	3
47 611.683	7.914	1.945	0.458	0.989	1.389	1.189	1.528	2	3
47 612.650	7.922	1.960	0.464	0.997	1.390	1.194	1.529	2	2
47 613.630	7.908	1.946	0.463	0.985	1.393	1.202	1.544	2	3
47 614.616	7.940	1.960	0.444	0.994	1.387	1.181	1.522	2	2
47 636.622	7.917	1.926	0.469	0.988	1.391	1.201	1.539	3	3
47 637.557	7.904	1.931	0.472	0.989	1.396	1.200	1.546	3	3
47 638.572	7.898	1.935	0.462	0.991	1.391	1.198	1.545	3	3
47 639.559	7.903	1.935	0.467	0.988	1.383	1.195	1.539	3	3
47 640.572	7.889	1.935	0.467	0.984	1.392	1.208	1.549	3	3
47 643.654	7.900	1.950	0.472	0.979	1.390	1.207	1.549	3	3
47 648.573	7.894	1.955	0.474	0.986	1.394	1.204	1.553	2	3
47 655.605	7.930	1.962	0.459	0.986	1.394	1.190	1.535	3	3
47 656.599	7.934	1.961	0.455	0.988	1.383	1.190	1.529	3	3
47 881.838	7.984	1.974	0.425	1.003	1.366	1.158	1.490	2	3
47 883.832	7.973	1.941	0.429	1.011	1.373	1.163	1.493	3	3
47 885.829	7.978	1.943	0.429	1.005	1.380	1.163	1.494	3	3
47 887.830	7.979	1.962	0.418	1.008	1.372	1.154	1.487	2	2
47 892.827	7.957	1.950	0.425	0.992	1.374	1.159	1.493	3	3
47 893.821	7.945	1.967	0.436	1.000	1.377	1.173	1.504	3	3
47 896.787	7.944	1.978	0.440	1.006	1.379	1.175	1.510	3	3
47 898.826	7.932	1.969	0.456	0.995	1.378	1.185	1.522	3	3
47 901.846	7.935	1.954	0.465	0.993	1.392	1.198	1.541	3	3
47 902.836	7.930	1.969	0.465	0.991	1.381	1.200	1.535	3	3
47 903.848	7.933	1.976	0.468	0.989	1.395	1.201	1.541	3	3
48 701.675	8.012	1.943	0.417	1.011	1.369	1.153	1.484	2	2

Table 6. continued.

HJD(24+)	V	$[U-B]$	$[V-B]$	$[B1-B]$	$[B2-B]$	$[V1-B]$	$[G-B]$	Weight(mag)	Weight(colour)
48 704.747	8.009	1.952	0.421	1.011	1.379	1.154	1.491	3	3
48 706.648	8.010	1.950	0.423	1.012	1.367	1.159	1.490	2	2
48 735.615	7.893	1.980	0.474	0.979	1.392	1.208	1.548	2	3
48 753.660	8.017	1.956	0.430	1.006	1.370	1.157	1.500	2	2
48 794.490	7.944	1.970	0.455	0.992	1.393	1.192	1.520	3	3
49 043.782	7.965	1.922	0.457	0.990	1.380	1.192	1.530	3	3
49 050.771	7.923	1.944	0.473	0.984	1.397	1.200	1.542	3	3
49 057.794	7.879	1.951	0.477	0.981	1.392	1.212	1.549	3	3
49 063.785	7.874	1.951	0.479	0.981	1.396	1.214	1.553	3	3
49 085.668	7.967	1.946	0.448	0.986	1.382	1.185	1.523	2	3
49 095.594	7.938	1.943	0.452	0.992	1.391	1.176	1.518	2	2
49 100.617	7.931	1.944	0.463	0.993	1.387	1.188	1.523	2	2
49 102.615	7.929	1.939	0.466	0.986	1.389	1.201	1.536	3	3
49 104.622	7.907	1.947	0.474	0.986	1.391	1.206	1.550	3	3
49 105.646	7.907	1.943	0.480	0.977	1.382	1.213	1.554	2	3
49 386.836	7.865	1.959	0.487	0.978	1.394	1.214	1.559	2	3
49 407.783	7.967	1.960	0.452	0.996	1.387	1.182	1.520	3	3
49 414.851	7.993	1.937	0.422	1.001	1.367	1.160	1.487	3	3
49 426.796	7.966	1.921	0.421	0.997	1.373	1.159	1.487	3	3
49 451.758	7.913	1.951	0.480	0.978	1.395	1.209	1.558	3	3
49 454.771	7.935	1.935	0.469	0.988	1.388	1.202	1.536	3	3
49 456.751	7.942	1.941	0.458	0.990	1.381	1.188	1.529	3	3
49 459.723	7.965	1.955	0.434	0.992	1.372	1.166	1.505	3	3
49 460.733	7.970	1.939	0.433	1.000	1.384	1.168	1.498	2	2
49 468.725	7.976	1.941	0.437	1.003	1.381	1.170	1.500	3	3
49 513.584	7.931	1.940	0.446	0.995	1.383	1.175	1.513	3	3
49 521.566	7.929	1.936	0.454	0.990	1.387	1.186	1.519	3	3
49 524.543	7.937	1.940	0.452	0.994	1.392	1.194	1.522	4	3
49 794.742	7.937	1.968	0.469	1.001	1.387	1.199	1.536	2	3
49 796.724	7.935	1.969	0.445	0.996	1.385	1.183	1.518	2	2
49 798.764	7.950	1.948	0.447	0.991	1.386	1.179	1.518	3	3
49 800.749	7.965	1.961	0.449	0.997	1.382	1.179	1.515	3	3
49 802.707	7.968	1.960	0.448	0.997	1.385	1.179	1.518	3	2
49 806.613	7.958	1.946	0.441	0.995	1.379	1.181	1.515	3	2
49 808.725	7.962	1.949	0.433	0.996	1.376	1.173	1.500	2	1
49 831.651	7.898	1.948	0.485	0.976	1.395	1.216	1.560	2	3
49 833.676	7.899	1.954	0.487	0.980	1.395	1.220	1.559	3	3
49 836.630	7.904	1.964	0.487	0.974	1.394	1.217	1.554	3	2
49 839.679	7.911	1.965	0.484	0.982	1.390	1.214	1.558	3	3
49 841.517	7.928	1.965	0.485	0.981	1.397	1.210	1.554	3	3
49 846.663	7.939	1.952	0.476	0.996	1.401	1.207	1.543	3	3
49 851.661	7.970	1.939	0.449	0.995	1.386	1.189	1.525	3	3
49 853.656	7.966	1.954	0.451	0.994	1.384	1.183	1.520	3	2
50 109.846	8.002	1.939	0.415	1.013	1.362	1.154	1.474	3	3
50 112.858	8.019	1.933	0.413	1.017	1.381	1.144	1.470	3	3
50 115.801	8.020	1.935	0.414	1.007	1.369	1.143	1.476	3	3
50 116.850	8.018	1.933	0.420	1.009	1.371	1.147	1.483	3	3
50 119.853	7.995	1.923	0.429	1.003	1.380	1.163	1.494	3	2
50 121.851	8.000	1.927	0.425	0.998	1.369	1.157	1.482	3	3
50 123.859	7.972	1.932	0.434	0.999	1.377	1.166	1.500	2	2
50 124.864	7.962	1.945	0.445	0.994	1.381	1.186	1.520	3	3
50 125.849	7.954	1.938	0.449	0.992	1.386	1.188	1.523	3	3
					EN TrA				
47 608.812	8.885	2.154	−0.086	1.151	1.242	0.680	0.897	3	3
47 608.817	8.891	2.112	−0.078	1.158	1.242	0.681	0.905	3	3
47 609.759	8.903	2.078	−0.066	1.151	1.250	0.695	0.912	2	3
47 610.756	8.908	2.056	−0.048	1.142	1.255	0.715	0.936	2	3
47 611.793	8.923	2.061	−0.035	1.123	1.255	0.720	0.942	2	3
47 612.785	8.905	2.021	−0.013	1.123	1.264	0.747	0.974	2	2
47 614.822	8.859	2.020	0.032	1.116	1.286	0.789	1.021	2	2
47 636.730	8.477	2.029	0.028	1.116	1.279	0.780	1.021	3	3
47 637.730	8.489	2.032	0.020	1.098	1.278	0.776	1.014	3	3
47 638.678	8.510	2.039	0.026	1.110	1.279	0.784	1.015	3	3
47 639.670	8.530	2.031	0.027	1.115	1.286	0.784	1.022	3	3
47 640.677	8.558	2.042	0.028	1.106	1.281	0.785	1.025	3	3
47 643.718	8.606	2.002	0.063	1.084	1.301	0.817	1.065	3	3
47 648.707	8.651	1.979	0.145	1.060	1.328	0.898	1.157	2	3

Table 6. continued.

HJD(24+)	V	$[U-B]$	$[V-B]$	$[B1-B]$	$[B2-B]$	$[V1-B]$	$[G-B]$	Weight(mag)	Weight(colour)
47 655.679	8.509	1.972	0.217	1.045	1.345	0.967	1.239	3	3
47 656.686	8.503	1.970	0.199	1.038	1.342	0.947	1.221	3	3
48 099.521	8.614	1.993	0.201	1.039	1.335	0.942	1.207	2	2
48 101.491	8.567	1.986	0.249	1.010	1.347	0.989	1.266	3	3
48 103.496	8.554	2.002	0.257	1.019	1.368	0.996	1.282	2	2
48 105.510	8.582	2.002	0.226	1.036	1.349	0.965	1.251	2	2
48 113.524	8.727	2.031	−0.004	1.123	1.268	0.753	0.985	3	3
48 117.533	8.763	2.119	−0.091	1.159	1.232	0.669	0.881	3	3
48 133.582	9.088	2.112	−0.093	1.169	1.258	0.671	0.875	3	3
48 339.736	8.698	2.082	−0.050	1.143	1.258	0.718	0.934	2	2
48 342.766	8.727	2.106	−0.065	1.157	1.248	0.699	0.922	3	3
48 349.795	8.804	2.092	−0.042	1.141	1.247	0.717	0.943	2	2
48 371.721	8.562	2.043	0.111	1.082	1.304	0.863	1.109	3	3
48 374.709	8.605	2.071	0.033	1.109	1.283	0.792	1.030	2	2
48 377.715	8.645	2.102	−0.008	1.126	1.270	0.753	0.990	3	3
48 384.677	8.812	2.102	−0.079	1.158	1.246	0.684	0.904	3	3
48 389.716	8.932	2.064	−0.082	1.149	1.253	0.679	0.896	3	3
48 735.757	8.536	2.007	0.174	1.052	1.329	0.922	1.195	2	3
48 736.731	8.536	2.021	0.155	1.057	1.331	0.912	1.171	2	3
48 793.619	8.729	2.071	−0.030	1.131	1.254	0.724	0.960	2	3
49 049.872	8.673	2.042	−0.019	1.126	1.257	0.736	0.975	3	3
49 054.849	8.816	1.974	0.022	1.103	1.282	0.780	1.016	3	3
49 057.852	8.811	1.962	0.057	1.084	1.310	0.819	1.066	3	3
49 060.845	8.711	1.937	0.111	1.057	1.317	0.863	1.117	3	3
49 063.832	8.594	1.942	0.150	1.059	1.326	0.899	1.163	3	3
49 085.770	8.627	2.045	0.016	1.132	1.290	0.772	1.010	2	3
49 411.874	8.559	2.047	−0.016	1.130	1.264	0.748	0.970	3	3
49 412.877	8.589	2.045	−0.008	1.124	1.269	0.753	0.988	3	2
49 415.878	8.647	2.033	0.000	1.117	1.275	0.755	0.997	3	3
49 422.856	8.707	1.968	0.133	1.063	1.326	0.885	1.138	2	2
49 426.858	8.563	1.963	0.225	1.028	1.347	0.966	1.254	3	3
49 451.801	8.815	2.151	−0.150	1.181	1.215	0.619	0.817	3	3
49 456.805	8.972	2.132	−0.112	1.173	1.237	0.660	0.858	3	3
49 468.714	8.526	1.988	0.181	1.052	1.331	0.942	1.198	3	3
49 513.624	8.528	2.078	−0.002	1.122	1.263	0.757	0.992	3	3
49 521.676	8.646	2.113	−0.111	1.173	1.235	0.655	0.872	3	3
49 797.816	8.589	1.996	0.221	1.032	1.352	0.977	1.248	3	3
49 800.806	8.617	2.022	0.171	1.044	1.332	0.928	1.179	3	3
49 803.814	8.654	2.052	0.080	1.086	1.306	0.837	1.087	2	2
49 807.796	8.649	2.050	0.008	1.117	1.276	0.772	0.999	3	3
49 831.731	8.647	1.995	0.200	1.042	1.341	0.959	1.219	2	3
49 837.720	8.665	1.986	0.102	1.073	1.308	0.870	1.115	3	2
49 839.734	8.682	2.008	0.058	1.092	1.298	0.817	1.049	3	3
49 841.720	8.695	2.022	0.013	1.108	1.281	0.770	1.001	3	3
49 846.695	8.715	2.110	−0.077	1.162	1.250	0.688	0.902	3	3
49 851.684	8.799	2.052	−0.117	1.170	1.240	0.648	0.859	3	3
49 853.672	8.830	2.057	−0.119	1.165	1.237	0.644	0.865	3	2
IRAS 19125+0343									
52 415.66975	10.230	2.381	−0.163	1.033	1.323	0.610	0.791	3	3
524 317.69291	10.238	2.387	−0.153	1.039	1.338	0.622	0.799	3	3
524 219.69850	10.233	2.399	−0.167	1.026	1.315	0.609	0.784	2	2
524 321.66363	10.268	2.372	−0.164	1.036	1.323	0.615	0.773	2	3
524 322.68742	10.269	2.360	−0.173	1.029	1.303	0.600	0.775	3	3
524 327.67544	10.283	2.396	−0.178	1.042	1.317	0.602	0.761	2	3
524 328.67778	10.289	2.409	−0.177	1.050	1.318	0.598	0.771	3	3
524 329.68165	10.286	2.418	−0.176	1.041	1.320	0.601	0.766	2	3
524 251.60071	10.234	2.426	−0.159	1.034	1.333	0.613	0.799	3	2
524 352.60556	10.234	2.421	−0.163	1.021	1.332	0.624	0.794	2	3
524 253.62684	10.242	2.442	−0.161	1.038	1.324	0.614	0.798	2	2
524 354.62246	10.255	2.460	−0.156	1.043	1.339	0.612	0.794	3	3
524 355.62875	10.247	2.419	−0.161	1.040	1.317	0.608	0.779	2	3
524 256.61663	10.258	2.427	−0.167	1.056	1.334	0.606	0.787	3	2
524 358.61192	10.273	2.413	−0.164	1.044	1.324	0.598	0.784	2	3
524 376.52627	10.214	2.427	−0.181	1.030	1.312	0.608	0.786	3	3
524 288.51420	10.216	2.413	−0.160	1.030	1.335	0.606	0.799	2	2

Table 6. continued.

HJD(24+)	V	$[U-B]$	$[V-B]$	$[B1-B]$	$[B2-B]$	$[V1-B]$	$[G-B]$	Weight(mag)	Weight(colour)
524 391.52369	10.223	2.407	−0.156	1.047	1.334	0.617	0.796	2	3
524 392.47117	10.232	2.385	−0.159	1.045	1.333	0.625	0.797	3	3
524 293.49170	10.234	2.400	−0.160	1.031	1.342	0.623	0.796	3	2
524 399.46539	10.259	2.388	−0.167	1.037	1.333	0.607	0.785	2	3
525 301.45406	10.260	2.405	−0.170	1.030	1.307	0.610	0.781	2	3
525 305.47919	10.275	2.456	−0.168	1.040	1.327	0.606	0.777	3	3
525 306.47941	10.268	2.516	−0.178	1.039	1.325	0.590	0.771	3	3
525 330.42345	10.214	2.402	−0.161	1.030	1.337	0.621	0.786	2	3
525 261.38422	10.218	2.385	−0.162	1.045	1.343	0.617	0.794	2	2
528 319.61978	10.219	2.359	−0.137	1.024	1.331	0.628	0.808	3	3
528 322.61384	10.220	2.360	−0.134	1.019	1.338	0.631	0.829	3	3
528 325.61868	10.230	2.361	−0.136	1.022	1.339	0.632	0.816	2	3
528 352.54597	10.243	2.464	−0.160	1.052	1.332	0.615	0.788	3	3
528 353.50173	10.261	2.452	−0.156	1.042	1.332	0.614	0.788	3	3
528 354.48603	10.249	2.448	−0.167	1.054	1.330	0.620	0.787	2	3
528 456.50272	10.240	2.453	−0.162	1.046	1.325	0.606	0.790	3	4
535 390.49430	10.244	2.412	−0.142	1.033	1.335	0.630	0.807	2	3
535 393.51927	10.233	2.423	−0.154	1.038	1.350	0.621	0.805	2	3
535 394.52526	10.247	2.395	−0.149	1.038	1.334	0.623	0.808	4	3
535 395.52349	10.242	2.380	−0.153	1.035	1.328	0.627	0.798	4	3
536 206.48002	10.265	2.393	−0.169	1.023	1.328	0.601	0.782	2	2
IRAS 19157-0247									
52446.63893	10.725	2.290	−0.015	1.006	1.332	0.751	0.964	1	3
52501.50119	10.742	2.339	−0.051	1.033	1.351	0.712	0.911	2	3
52502.46879	10.749	2.351	−0.060	1.026	1.356	0.713	0.903	2	3
52505.44584	10.775	2.332	−0.056	1.026	1.346	0.716	0.921	3	3
52507.43737	10.753	2.290	−0.041	1.012	1.358	0.722	0.941	2	1
52561.39041	10.688	2.278	−0.002	1.004	1.368	0.778	0.969	3	3